Energy and AI 20 (2025) 100493

Contents lists available at ScienceDirect

Energy and AI

journal homepage: www.elsevier.com/locate/egyai

Physics-constrained transfer learning: Open-circuit voltage curve reconstruction and degradation mode estimation of lithium-ion batteries

Tobias Hofmann [a,b,*], Jacob Hamar [b], Bastian Mager [b], Simon Erhard [b], Jan Philipp Schmidt [a]

[a] *Chair of Systems Engineering for Electrical Energy Storage (SysEE), University of Bayreuth, Bavarian Center for Battery Technology (BayBatt), Universitätsstraße 30, Bayreuth, 95447, Bavaria, Germany*
[b] *BMW Group, Petuelring 130, Munich, 80809, Bavaria, Germany*

HIGHLIGHTS

- TCN-LSTM models accurately estimate DMs and OCV from partial charging voltage segments.
- Integrating the mechanistic model physically constrains the output.
- Transfer learning adapts models effectively across different cell types.
- Extensive testing across diverse use cases verifies model robustness.
- A single aging path suffices to fine-tune the models with high accuracy.

GRAPHICAL ABSTRACT

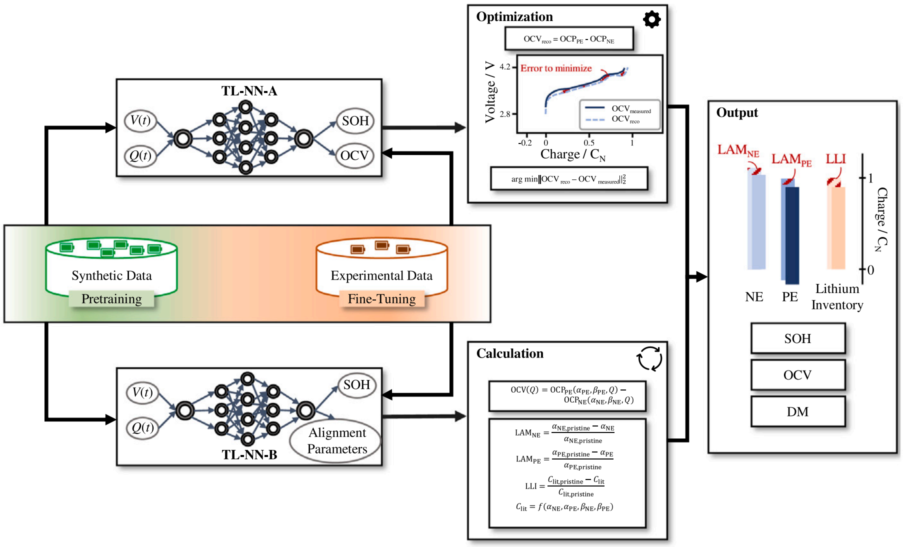

ARTICLE INFO

Keywords:
Lithium-ion battery
State of health estimation
Transfer learning
Degradation modes
Mechanistic model

ABSTRACT

Open-circuit voltage (OCV) updates are the key to accurate state of charge (SOC) estimates over lifetime. Degradation modes (DM) are directly coupled to OCV estimation. They offer a more detailed analysis of the battery's state of health (SOH) and yield optimized usage strategy, and with that, a prolonged lifetime. In this study two data-driven models are coupled with physics-based models and compared in regards of their OCV and DM estimation accuracy: Two temporal convolutional — long short-term memory neural networks (TCN-LSTM) are trained from synthetic NCA-graphite battery data for OCV curve estimation (model 1) and alignment parameter estimation (model 2). Both models are fine-tuned with varying amounts of experimental NMC-graphite battery data during the transfer learning (TL) step. In the subsequent physics-constraining part the DMs are derived via optimization (model 1), i.e., fitting the OCV with half cell open-circuit potentials, or

---

* Corresponding author at: Chair of Systems Engineering for Electrical Energy Storage (SysEE), University of Bayreuth, Bavarian Center for Battery Technology (BayBatt), Universitätsstraße 30, Bayreuth, 95447, Bavaria, Germany.
E-mail address: tobias1.hofmann@uni-bayreuth.de (T. Hofmann).

https://doi.org/10.1016/j.egyai.2025.100493
Received 27 September 2024; Received in revised form 6 February 2025; Accepted 3 March 2025

directly via mathematical equations (model 2). Both models prove that fine-tuning data from one aging path suffices, if it includes the maximum appearing DMs of the target domain. For these use cases both models maintain OCV mean absolute errors (MAEs), DM MAEs and SOH mean absolute percentage errors (MAPEs) under 10 mV, 3.10 % and 1.98 %, respectively. The model 2 has less computational complexity and reaches slightly better results but requires labeled target data including alignment parameters for its application. This study shows that synthetic data is eligible for TL, even for varying cell chemistries, and that the mechanistic model helps to physically constrain the output.

1. Introduction

In recent years the new registrations of battery electric vehicles (BEVs) have rapidly increased [1]. With that, more used BEVs are available on the aftermarket, where customers are especially interested in the SOH. The SOH is the currently available energy relative to its value at begin of life (BOL). The definition is usually simplified to the currently available capacity relative to its pristine value [2]. The battery is the most costly component of BEVs and, hence, it heavily defines the residual value. The SOH, however, is not only important when selling a BEV but rather mandatory over the whole vehicle lifetime to allow accurate SOC or remaining range estimations, efficient operation and healthy charging. OCV updates for BEVs, unfortunately, have not yet been well documented or reached a sufficient state of the art. Knowledge about the OCV, however, is crucial and the backbone of accurate state estimation. Due to its aging-path-dependent variation, maintaining high OCV reconstruction accuracy is challenging [3,4]. It, additionally, allows the calculation of DMs [5], which help to realize adaptive, aging-path-individual, usage strategies. Such counteractions may help to, e.g., reduce the time at high storage SOCs which prevents the battery from further triggering a specific DM and might lead to a knee point [6].

Throughout this research paper, we refer to the simplified SOH definition as the currently available capacity $Q(t)$ in relation to the available capacity in its initial state $Q(t_0)$, as given in

$$\mathrm{SOH}(t) = \frac{Q(t)}{Q(t_0)}. \tag{1}$$

The automotive industry has long sought effective data-driven approaches to estimate battery SOH. Recent advancements [7–13] in data-driven SOH estimation have shown promising results. Bockrath et al. [8], for example, used a TCN to estimate SOH from raw partial constant-current discharge segments, achieving an SOH root mean squared error (RMSE) of 1.0 % for the NASA dataset. Costa et al. [9] extended the field to include DM estimation using a convolutional neural network (CNN) with synthetic data, achieving an RMSE of 2 % for all DMs of interest. Yet, a key challenge remains: Determining the OCV, and consequently DMs, over the lifetime of non-synthetic battery data still requires costly and time-consuming aging experiments to parametrize these aging models, making it difficult to keep pace with the rapid development cycles of new battery generations. Novel approaches for OCV reconstruction from real-world charging events are sought more than ever. TL allows the usage of pretrained models and adopting them to small target datasets. There has been a significant increase in publications [14–26] exploiting TL for SOH, DM, or OCV estimation: Yao and Han [14] explored the influence of different aging paths in a CNN-TL model, achieving an SOH RMSE of 2.2 %. Zhou et al. [15] extended TL-based OCV reconstruction to other cell chemistries, achieving SOH RMSEs 0.47 % and 2.73 % for nickel cobalt aluminium oxide (NCA) and lithium iron phosphate (LFP) cells, respectively. Hofmann et al. [17] demonstrated that TL from synthetic data is possible across different cell chemistries with a mean absolute error (MAE) of 12 mV for OCV reconstruction and a mean absolute percentage error (MAPE) of 1.1 % for SOH. On the other hand, optimization models based on mechanistic approach [5] only require pristine measurements but are heavily limited by the input data's precision requirements [5,27–32].

The combination of data-driven and physics-based models is a promising research avenue to reduce data requirements and integrate physical constraints [33–41]. Liang et al. [34], for example, have merged two machine learning (ML) models and weighted their output based on a nonlinear optimization result. They have used time-series data from battery charging as an input for two models that both output the SOH. During the training phase an optimization process yielded the weights of each SOH estimate. The final estimated SOH reached a RMSE below 1 % but required full charging cycles to deploy. Tian et al. [25] have used partial charging voltage curves at 1C as an input for a CNN model that estimated the alignment parameters which directly yield the DMs, as well as the OCV curve. Their supervised learning approach required labels which were generated via optimization, i.e., minimizing the difference between reconstructed and measured OCV in repetitive checkups of aging tests. The RMSE of the reconstructed OCV from the CNN model remained below 15 mV.

Reviewing the state of the art, we identify a research gap in the field of physics-constrained ML for OCV curve reconstruction and DM estimation. While substantial progress has been made in the field of TL for SOH [34] and OCV estimation [17,25], there remains a gap in the integration of TL with physics-based optimization models for real-world applications. Existing studies treat TL and optimization separately, missing the opportunity to leverage the strengths of both approaches in a combined framework. Especially the usage of synthetic data for DM estimation has not been reported before. We present a novel approach that directly couples TL with optimization, leveraging the strengths of both methods. Our model uses a TCN-LSTM architecture to estimate the OCV curve from partial charging segments, followed by an optimization step to refine the OCV and calculate DMs. By pretraining our TL model with high-quality synthetic data and fine-tuning with minimal experimental data, we significantly reduce the data requirements and associated costs of aging experiments. The inclusion of an optimization step based on the mechanistic model ensures that the estimated OCV and DMs are physically consistent and accurate, addressing a key limitation of purely data-driven approaches. This approach is compared to an alternative path that uses the same architecture to directly estimate the alignment parameters, and from that reconstruct the OCV. Our approach is validated across different UCs, demonstrating its versatility and potential for real-world applications, including scenarios with limited and noisy data. In summary, our work bridges the gap between data-driven TL models and physics-based optimization, providing a robust and efficient solution for SOH and OCV estimation that is both data-efficient and physically consistent.

To our knowledge this is the first study to directly couple synthetic data, ML and optimization for OCV curve reconstruction and DM estimation. By comparing various model architectures and UCs we are able to evaluate the individual strengths of model parts and data requirements. The incorporation of synthetic data as the source domain for TL yields low data requirements, allows rapid reduction in aging experiment costs and development time for model parametrization. The inclusion of the optimization, based on the mechanistic model approach, however, integrates physical constraints and improves battery state estimation. Furthermore, the training of neural networks necessitates a large number of data points, which are often unavailable in the early stages due to cost and time constraints associated with aging experiments. By supplementing limited experimental data with synthetic data that mirrors physical behavior, these limitations can be overcome. This paper specifically investigates the utility and boundaries of synthetic data in this context by addressing key questions such as the optimal ratio of synthetic to real data, the required similarity between synthetic and real data, and the feasibility of extrapolation.

2. Theory

The combination of simulation, ML and optimization allows the generation of mass data, learning from that data and finally fusing the output with physico-chemical information from pristine half-cell potential curves. Hence, we introduce the basics of the used simulation toolbox (mechanistic model), the ML framework (TL) and the optimization (OCV reconstruction). For a more detailed description of the mechanistic model, TL, and optimization, we refer to previous publications [17,27]. While our prior work [17] established the theoretical foundation for the neural networks (NNs) and TL techniques used, this section introduces the novel aspects of our approach. Specifically, we emphasize the integration of the OCV model with the calculation of DMs through mathematical optimization. This unique combination ensures both accuracy and physical consistency in OCV and DM estimations. Nevertheless, the essential theoretical basics are briefly reintroduced for completeness.

2.1. Mechanistic model for battery data generation

Dubarry et al. [5] have introduced the mechanistic model approach as a simplification for battery degradation which breaks down the complex mechanisms to relative shifts and scalings between the open-circuit half-cell potential curves of the negative electrode (NE) $\mathrm{OCP_{NE}}$ and positive electrode (PE) $\mathrm{OCP_{PE}}$. These relative shifting and scaling can be determined by the alignment parameter set ϑ which is the set of scaling α_{NE}, α_{PE} and shifting parameters β_{NE}, β_{PE}. The resulting OCV is the difference between the positive and the negative open-circuit half-cell potential curve within its voltage boundaries

$$\begin{aligned}\mathrm{OCV}(Q) &= f(\mathrm{OCP_{NE}}, \mathrm{OCP_{PE}}, \vartheta, Q)\\ &= \mathrm{OCP_{PE}}(\alpha_{\mathrm{PE}}, \beta_{\mathrm{PE}}, Q) - \mathrm{OCP_{NE}}(\alpha_{\mathrm{NE}}, \beta_{\mathrm{NE}}, Q)\end{aligned} \tag{2}$$

where Q is the charge throughput. Eq. (2) can be applied to higher C-rates by exchanging the open-circuit half-cell potential curves with half-cell potential curves gathered at the desired C-rates. This implies that Eq. (2) transforms to

$$\begin{aligned}\mathrm{V}_{x\mathrm{C}}(Q) &= f(\mathrm{P}_{\mathrm{NE},x\mathrm{C}}, \mathrm{P}_{\mathrm{PE},x\mathrm{C}}, \vartheta, Q)\\ &= \mathrm{P}_{\mathrm{PE},x\mathrm{C}}(\alpha_{\mathrm{PE}}, \beta_{\mathrm{PE}}, Q) - \mathrm{P}_{\mathrm{NE},x\mathrm{C}}(\alpha_{\mathrm{NE}}, \beta_{\mathrm{NE}}, Q)\end{aligned} \tag{3}$$

with the half-cell potential curves $\mathrm{P_{NE,xC}}$, $\mathrm{P_{PE,xC}}$ at a given C-rate xC. Simulation toolboxes, e.g., the alawa-toolbox [5], exploit this theory to generate synthetic voltage charging curves at arbitrary degradation states (via ϑ) and C-rates (via xC).

The alignment parameter set ϑ directly transfers to the physico-chemical DMs with the following formula: The loss of active material (LAM) is the lost electrode capacity in relation to its pristine state.

$$\mathrm{LAM_{NE}} = \frac{\alpha_{\mathrm{NE,pristine}} - \alpha_{\mathrm{NE}}}{\alpha_{\mathrm{NE,pristine}}} \tag{4}$$

$$\mathrm{LAM_{PE}} = \frac{\alpha_{\mathrm{PE,pristine}} - \alpha_{\mathrm{PE}}}{\alpha_{\mathrm{PE,pristine}}} \tag{5}$$

The loss of lithium-inventory (LLI), however, is the lost cyclable lithium inventory, i.e., the superposition of both half-cell potential curves.

$$\mathrm{LLI} = \frac{C_{\mathrm{lit,pristine}} - C_{\mathrm{lit}}}{C_{\mathrm{lit,pristine}}} \tag{6}$$

The available lithium inventory C_{lit} demands a case-sensitive definition [27].

$$C_{\mathrm{lit}} = \begin{cases} (\alpha_{\mathrm{PE}} - \beta_{\mathrm{NE}} + \beta_{\mathrm{PE}}) \cdot C_{\mathrm{N}} & \text{, for} \quad (\alpha_{\mathrm{PE}} - \beta_{\mathrm{NE}} + \beta_{\mathrm{PE}}) < \alpha_{\mathrm{NE}} \\ & \wedge \quad (\beta_{\mathrm{PE}} - \beta_{\mathrm{NE}}) \leq 0 \\ (\alpha_{\mathrm{NE}}) \cdot C_{\mathrm{N}} & \text{, for} \quad (\alpha_{\mathrm{PE}} - \beta_{\mathrm{NE}} + \beta_{\mathrm{PE}}) > \alpha_{\mathrm{NE}} \\ & \wedge \quad (\beta_{\mathrm{PE}} - \beta_{\mathrm{NE}}) \leq 0 \\ (\alpha_{\mathrm{NE}} + \beta_{\mathrm{NE}} - \beta_{\mathrm{PE}}) \cdot C_{\mathrm{N}} & \text{, for} \quad (\alpha_{\mathrm{NE}} + \beta_{\mathrm{NE}} - \beta_{\mathrm{PE}}) < \alpha_{\mathrm{PE}} \\ & \wedge \quad (\beta_{\mathrm{PE}} - \beta_{\mathrm{NE}}) \geq 0 \\ (\alpha_{\mathrm{PE}}) \cdot C_{\mathrm{N}} & \text{, for} \quad (\alpha_{\mathrm{NE}} + \beta_{\mathrm{NE}} - \beta_{\mathrm{PE}}) > \alpha_{\mathrm{PE}} \\ & \wedge \quad (\beta_{\mathrm{PE}} - \beta_{\mathrm{NE}}) \geq 0 \end{cases} \tag{7}$$

2.2. Open-circuit voltage reconstruction via optimization

The mechanistic model approach can be used to reconstruct the OCV and determine the underlying DMs from either full or partial (pseudo) OCV measurements [28–30]. The process of this optimization workflow is displayed in Fig. 1. Fig. 1(a) shows the necessary input, namely the measured and normalized pristine electrode open-circuit potential (OCP) curves $\mathrm{OCP_{NE}}$ and $\mathrm{OCP_{PE}}$ and the measured and normalized $\mathrm{OCV_{measured}}$. Many different solvers can be used for optimization, with least-squares being the most prominent [42]. Boundaries, as stated in Eq. (8), should be set for improved performance [27]. Fig. 1(b) presents the optimization itself. The solver aims to find the optimum parameter set $\vartheta = [\alpha_{\mathrm{NE}}, \alpha_{\mathrm{PE}}, \beta_{\mathrm{NE}}, \beta_{\mathrm{PE}}]$ that minimizes the discrepancy between the measured $\mathrm{OCV_{measured}}$ and the reconstructed $\mathrm{OCV_{reco}}$. For every possible alignment parameter set, the reconstructed OCV is simply calculated by Eq. (2).

The final optimization problem states as follows

$$\begin{aligned}\vartheta_{\mathrm{est}} &= \arg\min_{\vartheta} \|\mathrm{OCV_{measured}}(Q) - \mathrm{OCV_{reco}}(Q)\|_2^2\\ &= \arg\min_{\vartheta} \|\mathrm{OCV_{measured}}(Q) - f(\mathrm{OCP_{NE}}, \mathrm{OCP_{PE}}, \vartheta, Q)\|_2^2\\ \text{s.t.} \quad & \vartheta \geq \mathrm{lb}\\ & \vartheta \leq \mathrm{ub}\\ & f_{\mathrm{eq}}(\vartheta, \mathrm{OCV_{measured}}, \mathrm{OCV_{reco}}, ..) = 0\\ & f_{\mathrm{ineq}}(\vartheta, \mathrm{OCV_{measured}}, \mathrm{OCV_{reco}}, ..) \geq 0\end{aligned} \tag{8}$$

with lb and ub being the lower and upper boundaries, and $f_{\mathrm{eq}}(\vartheta, \mathrm{OCV_{measured}}, \mathrm{OCV_{reco}}, ..)$ and $f_{\mathrm{ineq}}(\vartheta, \mathrm{OCV_{measured}}, \mathrm{OCV_{reco}}, ..)$ as the equality and inequality constraints. The constraints can be any arbitrary functions that can be calculated from the available input. Fig. 1(c) finally visualizes the output of the method, based on the reconstructed OCV, including the SOH which is the available charge throughput within the voltage limits in comparison to its pristine values, and the DMs. With the help of Fig. 1(c) the DMs can be interpreted visually: The LAM is the decreased length of the electrode capacities and the LLI is the reduction in the overlapping section of both electrodes. Mathematically, Eqs. (4) to (7) are used to determine the DMs.

2.3. Transfer learning for battery state of health estimation

Supervised learning with NNs for battery state estimation, including SOH and DMs, and OCV reconstruction was extensively studied in available literature [7–13,15]. Supervised learning methods, however, rely on huge labeled training data, which are rare for the battery use case. For conventional methods, the training data must be representative for the target data, which further reduces suitable data. TL with NNs relaxes the strict requirements for training data.

In the context of TL, a domain $\mathcal{D}$ is formally defined as $\mathcal{D} = \{\chi, P(X)\}$, where χ represents the feature space and $P(X)$ denotes the edge probability distribution, with $X = \{x_1, \ldots, x_n\} \in \chi$ [17,43,44]. Similarly, a task $\mathcal{T}$ is defined as $\mathcal{T} = \{y, f(x)\}$, comprising the label space y and the target prediction function $f(x)$, which can also be

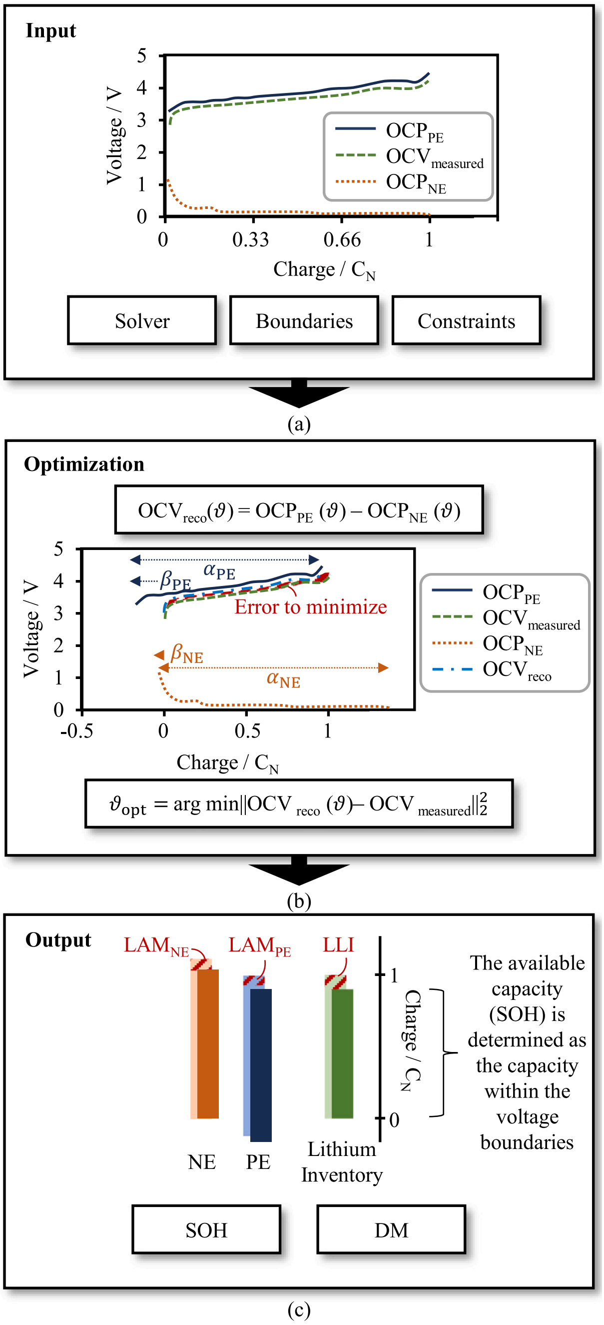

(a)

(b)

(c)

Fig. 1. Pipeline of OCV reconstruction via optimization. (a) Input, (b) Optimization, (c) Output.

interpreted as the conditional probability function $P(y \mid x)$ [17,43,44]. The number of samples within the source domain s and target domain t are given by N_s and N_t.

Definition 2.1 (*Transfer Learning*). The goal of TL is to improve the performance of the predictive function $f_{\mathcal{T}}()$ for the primary learning task $\mathcal{T}_t$. This is achieved by leveraging the latent knowledge discovered from a supplementary learning task $\mathcal{T}_s$ and its associated data $\mathcal{D}_s$, where $\mathcal{D}_s \neq \mathcal{D}_t$ and/or $\mathcal{T}_s \neq \mathcal{T}_t$, typically with $N_s \gg N_t$ [17,43,44].

Several types of TL exist, whereas for our problem at hand, parameter-based TL in the context of model-based TL is the most promising [17, 33,44]. Parameter-based TL refers to methods with domain adaption, i.e., $\mathcal{D}_s \neq \mathcal{D}_t$. In parameter-based TL a model gets pretrained in the source domain and reuses its learned parameters in the target domain. This is realized by, e.g., partial freezing and/or fine-tuning [44]. Some layers of the NN keep their weights, while some layers, mostly the output layer(s) [44], adopt their weights during fine-tuning with a reduced learning rate and/or reduced epochs. It is important to only allow small modifications of the network to avoid catastrophic forgetting, which describes an overfitted model to the target domain which has lost its memory of the source domain [44].

2.4. Performance metrics

The accuracy of the developed methods in terms of SOH, DM or OCV is measured with the MAE and MAPE

$$\text{MAPE} = \frac{1}{N}\sum_{i=1}^{N}\left|\frac{y_i - \hat{y}_i}{y_i}\right| \cdot 100\,\% \tag{9}$$

$$\text{MAE} = \frac{1}{N}\sum_{i=1}^{N}\left|y_i - \hat{y}_i\right| \tag{10}$$

where y_i is the true label and $\hat{y}_i$ is the estimated label of sample i. The total number of samples is N. Both, the MAE and the MAPE, are given in percent. The MAPE is generally useful to compare the SOH estimation accuracy across varying degradation states, because the SOH in the used data never approaches zero, which would drastically bias the MAPE [45]. The MAE, on the other hand, works for near-zero estimates and does not show this bias. Hence, the MAE is used for DM estimation accuracy. For better interpretability, the MAE is selected for the OCV reconstruction accuracy. Note that the OCV error is only calculated at the overlapping sections of the estimated and real capacity range. Hence, the MAE$_{\text{OCV}}$ must always be interpreted together with the MAPE$_{\text{SOH}}$.

3. Materials and method

Our research compares two methods which both combine model-based TL with the mechanistic model approach, as can be seen in Fig. 2. The TL-NN-A builds upon our previous work [17] but extends the approach to correct the OCV via optimization which enables the estimations of DMs. The TL-NN-B, on the other hand, utilizes the same data but the prior TL model is trained to directly output the scalar values SOH and the alignment parameters. From these values it is directly possible to calculate the OCV curve without the subsequent optimization step from the first approach.

3.1. Data

In our study, we use simulation data from an automotive prismatic NCA-graphite cell with 70.2 Ah capacity. This specific choice allows us to maintain consistency with our previous work [17] and directly compare the results. Furthermore, our previous findings indicate that the selection of simulation data type has minimal impact on the outcomes, provided that essential characteristics such as gradient changes within the voltage slope and sufficient sample diversity are present. This reinforces the robustness of our TL approach across different cell chemistries and configurations. Simulation data for the source domain is generated by a physico-chemical mechanistic model toolbox. The simulation toolbox takes the DMs and a constant-current C-rate as input, and outputs the voltage curve, charge throughput during charging, OCV curve, charge throughput for the OCV curve, SOH, and DMs. For more details about the cell characteristics and the simulation we refer to our previous publication [17]. One of the key findings in our previous work [17] was that the source domain in TL should encompass a larger search space than the target domain. To fulfill this requirement for any possible output variable, we add additional simulation data to the source domain, including more aging paths and C-rates. We add the

Table 1

The experimental data, taken from Schmitt et al. [28], which includes ten identical cells without any pre-treatment. For each cell the aging condition as well as the final SOH, DM fade, charge throughput and experiment duration is given.

Cell	Aging condition	ΔSOH	$\Delta\mathrm{LAM}_{\mathrm{NE}}$	$\Delta\mathrm{LAM}_{\mathrm{PE}}$	ΔLLI	Charge throughput	Duration
A1	Cycling (2.5 V–4.2 V)	30 %	30 %	15 %	35 %	6610 Ah	433 d
A2	Cycling (2.5 V–4.2 V)	30 %	30 %	15 %	35 %	5900 Ah	348 d
B1	Cycling (2.5 V–4.0 V)	15 %	15 %	8 %	15 %	8720 Ah	486 d
B2	Cycling (2.5 V–4.0 V)	15 %	15 %	8 %	15 %	8630 Ah	486 d
C1	Cycling (3.6 V–4.2 V)	15 %	15 %	8 %	15 %	6700 Ah	489 d
C2	Cycling (3.6 V–4.2 V)	15 %	15 %	8 %	15 %	7400 Ah	486 d
D1	Cycling (WLTP)	25 %	25 %	15 %	30 %	5210 Ah	489 d
D2	Cycling (WLTP)	25 %	25 %	15 %	30 %	5740 Ah	483 d
E1	Storage (3.7 V)	10 %	8 %	2.5 %	10 %	1530 Ah	454 d
E2	Storage (3.7 V)	10 %	8 %	2.5 %	10 %	1690 Ah	486 d

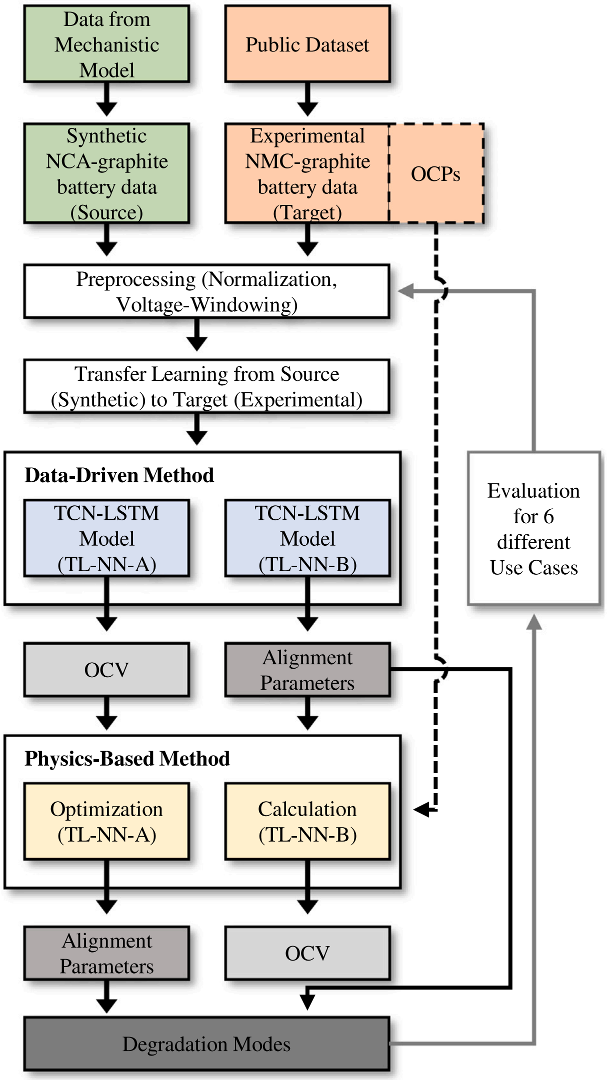

Fig. 2. Overview of the presented approach, from data generation and extraction to the coupling of data-driven and physics-based models.

C-rate of 3/2C to the simulation data, resulting in a total of seven C-rates: C/15, C/10, C/6, C/3, C/2, 1C and 3/2C. Besides that, we extend the aging path space by running simulations with each eight discrete steps in varying DMs. LAM is varied between 0 % and 40 %, while LLI is varied between 0 % and 60 %. In total 260 out of the possible 512 simulations are successful, due to constraints regarding the minimum voltage, and stored for later preprocessing. With these settings, the SOH ranges from 32.7 % to 100 % and in total $7 \cdot 260 = 1820$ samples are available.

The experimental data is taken from Schmitt et al. [28] and includes ten commercial INR18650 MJ1 nickel manganese cobalt oxide (NMC)-silicone/graphite cells with 3.35 Ah. As listed in Table 1, the cells were aged in five different scenarios. The aging test was performed for a total duration of maximum 489 d or until the cell surface temperature exceeded 60 °C at any time during the experiment. The operating ambient temperature during the experiment was set to 25 °C by a climate chamber. In the following we refer to the pseudo-OCV measurements as checkups, which took place during the reference performance test. The dataset not only includes the aging series of the ten cells, but also the pristine electrode potentials $\mathrm{OCP}_{\mathrm{NE}}$ and $\mathrm{OCP}_{\mathrm{PE}}$. A pristine cell was opened within an argon-filled glove box and coin cells with lithium-metal counter-electrodes were built. The used OCPs within this study are constant-current measurements at C/90 and an ambient temperature of 25 °C [46,47]. Table 1 not only includes the aging condition but also the resulting SOH and DM fade in the final checkup. The SOH was calculated by a pseudo-OCV measurement with C/30. It is defined as the capacity throughput within the voltage limits from 3.25 V to 4.2 V during these checkups, in which 3.25 V is the highest minimum value during all pseudo-OCV measurements of all cells. As explained by Schmitt et al. [28] the minimum voltage value of the charging pseudo-OCV curve increases over time, i.e., with rising impedance. To allow comparable results, the pseudo-OCV, as well as the SOH, is defined within these limited voltage boundaries. Because the DMs were not available in the published data [28], we generate these labels via optimization and the pristine OCP curves of the electrodes. In every checkup, the OCV curve is known and can be used to map the OCPs to the OCV and generate the DM labels via Eq. (4) to (7). The cost function combines the OCV with the DVA and ICA fit, because this has been shown to increase accuracy [48]. We refer to the measured and reconstructed DVA and ICA with $\mathrm{DVA}_{\mathrm{measured}}$, $\mathrm{DVA}_{\mathrm{reco}}$ and $\mathrm{ICA}_{\mathrm{measured}}$, $\mathrm{ICA}_{\mathrm{reco}}$, respectively. We use the scipy.optimize.minimize function with sequential least squares programming (SLSQP) and the default settings [49]. We exclude any additional constraints and solely pass upper and lower boundaries for the alignment parameter set ϑ. Hence, the optimization problem for one cell at iteration/checkup $i > 1$ is formulated as follows

$$\begin{aligned} \vartheta_{i,\mathrm{est}} = \arg\min_{\vartheta} \Bigg(& x_1 \left\| \frac{\mathrm{OCV}_{i,\mathrm{measured}} - \mathrm{OCV}_{i,\mathrm{reco}}}{\max(\mathrm{OCV}_{i,\mathrm{measured}})} \right\|_2^2 \\ & + x_2 \left\| \frac{\mathrm{DVA}_{i,\mathrm{measured}} - \mathrm{DVA}_{i,\mathrm{reco}}}{\max(\mathrm{DVA}_{i,\mathrm{measured}})} \right\|_2^2 \\ & + x_3 \left\| \frac{\mathrm{ICA}_{i,\mathrm{measured}} - \mathrm{ICA}_{i,\mathrm{reco}}}{\max(\mathrm{ICA}_{i,\mathrm{measured}})} \right\|_2^2 \Bigg) \\ \text{s.t.} \quad & \vartheta_{i,\mathrm{est}} \geq 0.8 \cdot \vartheta_{i-1,\mathrm{est}} \\ & \vartheta_{i,\mathrm{est}} \leq 1.1 \cdot \vartheta_{i-1,\mathrm{est}} \end{aligned} \tag{11}$$

with x_1 (OCV), x_2 (DVA) and x_3 (ICA) being 10, 1 and 1, respectively. These values were motivated by literature findings [48] and manually optimized to reach the lowest possible error. The components of the cost function are normalized to values below one for better interpretability of the weighting factors. The optimization runs for every cell individually and sets the boundaries depending on the last

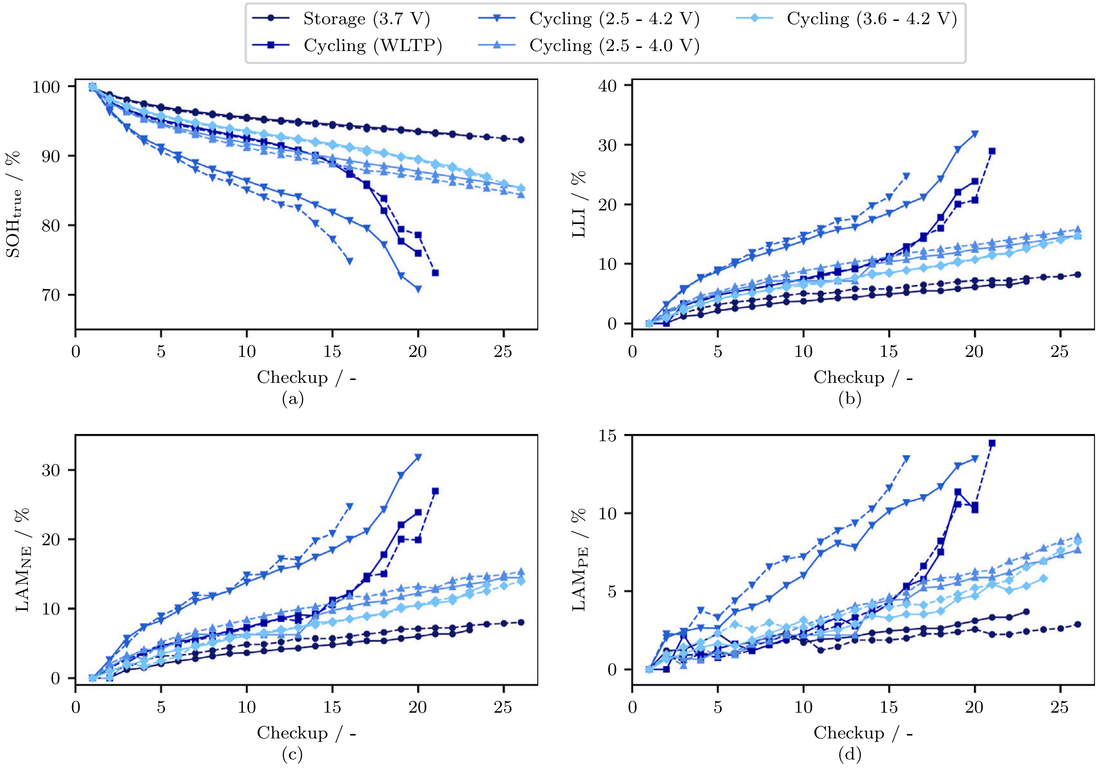

Fig. 3. The measured SOH (a) and estimated DMs ((b) LLI, (c) LAM$_{\mathrm{NE}}$, (d) LAM$_{\mathrm{PE}}$) from the OCV reconstruction of the experimental data.

iteration. The initial value is set to the optimization result from the previous iteration. For the initial run, the values for ϑ_0 are set to $[1.02, 1.14, -0.04, -0.14]$. The MAE$_{\mathrm{OCV}}$ stays below 3 mV for all samples along lifetime. The results of all checkups from all cells in regard to SOH and DMs is visualized in Fig. 3. One checkup took place approximately every 19 d. Each aging path includes two cells which mainly show very similar DMs over lifetime. All curves show good agreement with the visualized DMs in the publication by Schmitt et al. [28]. Note that they did not plot the DMs from checkups with a SOH below 80 %. As can be seen in Fig. 3(a), the partial cycling in the upper and lower region result in almost the same DMs at the final checkup. During the cycling, however, the cells cycled in the lower voltage region have shown higher degradation. Degrading the cell with full cycles lead to the highest degradation with a final SOH of approximately 70 %. The underlying DMs are higher than for any other aging condition. The WLTP cycling reaches similar DMs in the final checkup but showed a latter knee-point [6] after 15 checkups. In early checkups the cells behaved similar to those from the lower cycling phase. To analyze the influence of the checkups, a calendaric aging phase was conducted with cells stored at 3.7 V, 25 °C and the whole duration of the experiment (486 days) [28]. As expected, this aging phase has shown the least degradation and the SOH stays above 90 % for all checkups.

3.2. Method

The method overview is given by Fig. 2. Two models are developed with the same final output: The OCV, SOH and DMs. TL-NN-A directly estimates the OCV curve and feeds its output to an optimizer which fits the OCPs into the OCV curve to update its estimation and calculate the DMs. TL-NN-B does not require an optimization step because it estimates the alignment parameters. With these alignment parameters and the help of Eq. (2) and Eqs. (4) to (7) it is possible to calculate the OCV curve and also the DMs. Hence, the TL-NN-B approach offers an opportunity with less computational but stricter data requirements due to the explicit mandatory knowledge over all DMs.

Table 2
Selected voltage windows from the simulation and experimental data during preprocessing.

	V_{min}	V_{max}		V_{min}	V_{max}
Exp. Data	3.25 V	3.8 V	Sim. Data	2.8 V	3.8 V
	3.4 V	4.0 V		3.0 V	4.0 V
	3.6 V	4.1 V		3.2 V	4.1 V
	3.8 V	4.2 V		3.4 V	4.25 V
				3.6 V	
				3.8 V	

Table 3
Data size and input/output relation of both models. The estimated alignment parameters from TL-NN-B are reduced to $\vartheta_{\mathrm{reduced}}$, consisting of three values α_{NE}, α_{PE} and $\beta_{\mathrm{NE}} - \beta_{\mathrm{PE}}$ because these values include the same information but final complexity is reduced.

Signal	Dimension	TL-NN-A	TL-NN-B
$Q_{\mathrm{partial}}(t)$	$\mathbb{R}^{<1\times100>}$	Input	Input
$V_{\mathrm{partial}}(t)$	$\mathbb{R}^{<1\times100>}$	Input	Input
$I(t)$	$\mathbb{R}^{<1\times100>}$	Input	Input
$Q_{\mathrm{OCV}}(t)$	$\mathbb{R}^{<1\times100>}$	Output$_{\mathrm{TL}}$ Output$_{\mathrm{PB}}$	Output$_{\mathrm{PB}}$
OCV(t)	$\mathbb{R}^{<1\times100>}$	Output$_{\mathrm{TL}}$ Output$_{\mathrm{PB}}$	Output$_{\mathrm{PB}}$
SOH	$\mathbb{R}^{<1\times1>}$	Output$_{\mathrm{TL}}$ Output$_{\mathrm{PB}}$	Output$_{\mathrm{TL}}$ Output$_{\mathrm{PB}}$
DMs	$\mathbb{R}^{<1\times3>}$	Output$_{\mathrm{PB}}$	Output$_{\mathrm{PB}}$
$\vartheta_{\mathrm{reduced}}$	$\mathbb{R}^{<1\times3>}$		Output$_{\mathrm{TL}}$
ϑ	$\mathbb{R}^{<1\times4>}$	Output$_{\mathrm{PB}}$	

Both models process the same source and target domain. The data undergoes preprocessing which includes voltage windowing to later access the sensitivity of the models. The voltage windows are selected as in Table 2. Due to a larger voltage span in the simulation data, we extend the possible minimum voltages for this data. With these sampling, one simulation sample results in 23 windowed samples and one experimental sample in 15 windowed samples, respectively. In total, we thus create $1820\cdot 23 = 41860$ simulation data samples and $726\cdot 15 = 10890$ experimental data samples. Both datasets are individually normalized to lie in a range between zero and one. The data structure can be accessed in Table 3. In Table 3 Output$_{\text{TL}}$ refers to the output of a TL model and Output$_{\text{PB}}$ is the estimated physics-based value, either from the optimization model (TL-NN-A) or the calculated output via Eqs. (2) and (4) to (7) (TL-NN-B). The information loss between describing the alignment parameters as three instead of four variables is zero because the absolute value for β_{NE} can be accessed as the distance between the first value of the OCP$_{\text{NE}}$ curve and the minimum voltage of the full cell OCV curve. As shown in Table 3, both models utilize the same input from the partial charging segment: $Q_{\text{partial}}(t)$, $V_{\text{partial}}(t)$, and $I(t)$. The NN models are designed to process raw time-series signals without the need for feature processing or dimensionality reduction. The data-driven section of TL-NN-A directly generates the full OCV curve $Q_{\text{OCV}}(t)$ and OCV(t), from which the SOH can be determined as the maximum charge throughput between the voltage limits. In the subsequent optimization step, TL-NN-A again outputs the full OCV curve $Q_{\text{OCV}}(t)$ and OCV(t) along with the SOH. Additionally, this step allows for the calculation of DMs using the alignment parameters ϑ. Conversely, the data-driven section of TL-NN-B directly provides the SOH value and the reduced alignment parameters $\vartheta_{\text{reduced}}$. Through simple analytical equations, the complete TL-NN-B model can then compute the full OCV curve $Q_{\text{OCV}}(t)$ and OCV(t), as well as the DMs.

The study at hand determines the minimum requirements for fine-tuning data necessary for adequate generalization. Hence, six different UCs, as defined in Fig. 4, are introduced. In Fig. 4, the experimental data is categorized for each cell along with its respective aging path (compare with Table 1) and the applied C-rates during the checkups. In Sub Fig. 4(g), the simulation data only shows the applied C-rates and the division for pretraining. During pretraining, the objective is to learn as much as possible from the source domain. Consequently, except for the data at C/6 and C/3, the simulation data is directly used for training.

The UCs are separated into three categories (UC1, UC2 and UC3) which differ in the included aging path for the fine-tuning. In every category itself, the B UCs (Fig. 4(b), (d), (f)) aggravate the TL process by reducing the fine-tuning data even further in regards to the included C-rate. UC1A and UC1B (Fig. 4(a), (b)) include cells from aging path A (Cycling (2.5 V–4.2 V)), D (Cycling (WLTP)) and E (Storage (3.7 V)). Comparing with Table 1, it gets clear that these fine-tuning data, aging path A and D, show the highest degradation in terms of SOH and DMs and, hence, will be the easiest to apply TL. Fine-tuning data in UC2A and UC2B (Fig. 4(c), (d)) reduces to aging path A, which again shows the highest degradation and should allow successful TL. On the other side, UC3A and UC3B (Fig. 4(e), (f)) only include fine-tuning data from aging path B (Cycling (2.5 V–4.0 V)), which only shows a 15 % SOH drop. Hence, UC3A and UC3B are the most challenging tasks because their fine-tuning data from aging path B roughly shows half the degradation of aging path A.

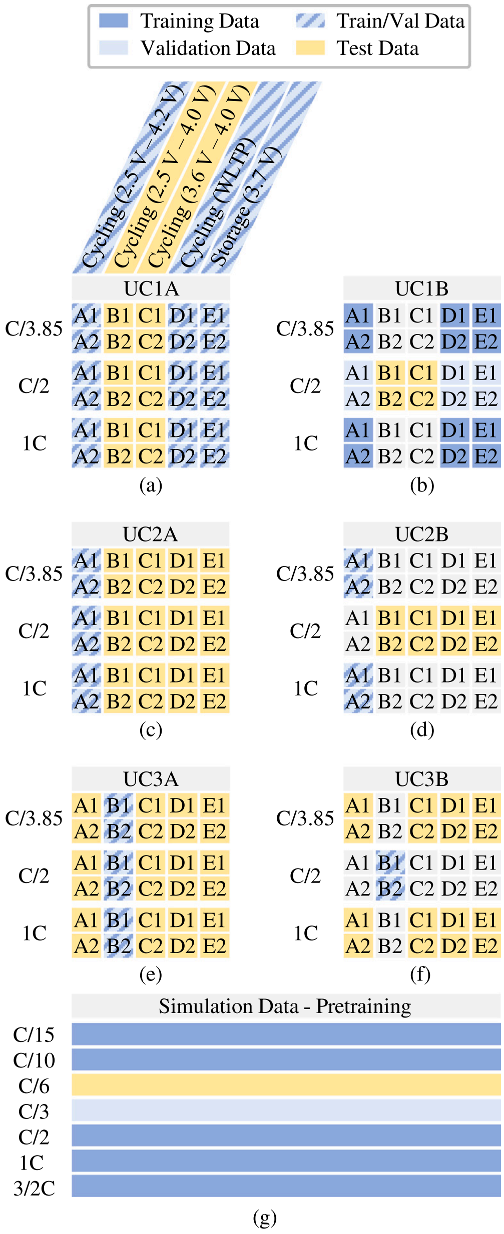

Fig. 4. Definition of use cases including data split for model training, validation and testing. (a) UC1A including the description of the relation between cell and the respective aging path, (b) UC1B, (c) UC2A, (d) UC2B, (e) UC3A, (f) UC3B, (g) simulation dataset used for pretraining. The used training data within each UC is displayed in dark blue, whereas the validation data is light blue. Both, training and validation data, are used for fine-tuning. The test data is yellow and if the data is excluded it is pictured white.

As outlined in Fig. 2, the prior model is a NN that either estimates the OCV curve (TL-NN-A) or directly estimates the alignment parameters (TL-NN-B). It is impossible to try every possible combination of available NN architectures to find the optimum. It is more efficient to tune the hyperparameters of a predefined architecture that has been shown to be advantageous for the given application in available literature [7,8,17,50–53]. TCNs have been found to be effective for time-series modeling as they can automatically extract relevant features from raw data [54]. Several studies have demonstrated the effectiveness of TCNs for SOH estimation [7,8,17,50–53]. In this work, we propose a hybrid approach that combines TCN layers as a feature extractor with subsequent LSTM layers as a feature interpreter. This approach is supported by previous research showing the mutual benefits of combining CNN with LSTM, and even TCN with LSTM [17,18,50,55]. The optimum hyperparameters are found via Bayesian optimization. Bayesian optimization is the state-of-the-art hyperparameter tuning method because it allows the exploration of large search spaces and the exploitation of promising valleys while being very efficient [17,56]. Bayesian optimization minimizes the required trials to find the optimum hyperparameter set because a surrogate model prunes unpromising directions and hence shrinks the search space continuously [17,56]. In this study, the KerasTuner [57] is used to optimize the NNs. Two different NNs, TL-NN-A and TL-NN-B, each adopted for six different UCs, are developed. The architecture tuning is limited to the source domain. The search space, however, stays consistent for every tuning operation and is listed in Table 4. In Table 4, for any hyperparameter λ for any layer N the possible set of values

Table 4
Search space for Bayesian hyperparameter tuning, where N refers to the layer number and λ is a hyperparameter that belongs to the set of possible hyperparameters Λ. Hence, for every additional TCN or LSTM layer, the respective hyperparameters can be tuned individually.

Hyperparameter	Definition
TCN layers	$\lambda_{\mathrm{TCN}} \in \Lambda_{\mathrm{TCN}}$ with $\Lambda_{\mathrm{TCN}} := \{\lambda_{\mathrm{TCN}} \in \mathbb{N}; 1 \le \lambda_{\mathrm{TCN}} \le 3\}$
Kernel Size	$\lambda_{\mathrm{K},N} \in \Lambda_{\mathrm{K}}$ with $\Lambda_{\mathrm{K}} := \{\lambda_{\mathrm{K}} \in \mathbb{N}; 1 \le \lambda_{\mathrm{K}} \le 8\}$
Filter Size	$\lambda_{\mathrm{F},N} \in \Lambda_{\mathrm{F}}$ with $\Lambda_{\mathrm{F}} := \{\lambda_{\mathrm{F}} \in \mathbb{N}; 8 \le \lambda_{\mathrm{F}} \le 128\}$
LSTM layers	$\lambda_{\mathrm{LSTM}} \in \Lambda_{\mathrm{LSTM}}$ with $\Lambda_{\mathrm{LSTM}} := \{\lambda_{\mathrm{LSTM}} \in \mathbb{N}; 0 \le \lambda_{\mathrm{LSTM}} \le 2\}$
Units	$\lambda_{\mathrm{U},N} \in \Lambda_{\mathrm{U}}$ with $\Lambda_{\mathrm{U}} := \{\lambda_{\mathrm{U}} \in \mathbb{N}; 8 \le \lambda_{\mathrm{U}} \le 128\}$
Dropout	$\lambda_{\mathrm{D},N} \in \Lambda_{\mathrm{D}}$ with $\Lambda_{\mathrm{D}} := \{\lambda_{\mathrm{D}} \in \mathbb{D}; 0 \le \lambda_{\mathrm{D}} \le 0.5\}$

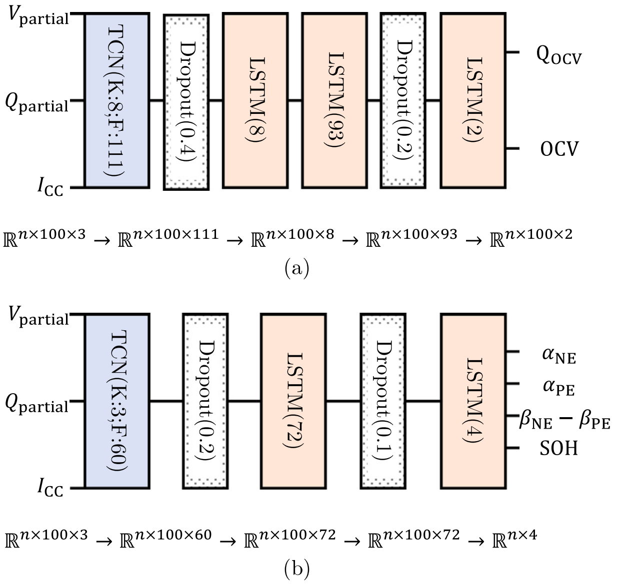

Fig. 5. Architecture of the optimized model for DM and SOH estimation, where (a) is the TL-NN-A and (b) is the TL-NN-B. In the TCN layers, K represents the kernel size and F the filter size.

is given by Λ. For any hyperparameter not listed in Table 4, we use the default parameter. Additionally, the models must end with a LSTM-layer which matches the output dimensions, i.e., two units for TL-NN-A and four units for TL-NN-B. All training run with the Adam optimizer [58]. The tuning process runs for 100 iterations with 60 initial points, a batch size of 128 and a maximum number of 500 epochs on a NVIDIA L4-2Q with 8 GB dedicated memory. One trial runs as long as the validation loss does not decrease for 50 consecutive epochs. Both TL-NNs use the data at C/3 from the simulation data as the validation data, the C/6 curves as the test data and the remaining simulation data serves as the training data. After successful tuning, the base TL-NNs are trained with the full simulation data in order to reach the optimum knowledge transfer. During this base-training process, 33 % of the simulation data are excluded from the training data and rather used as the validation data. The final architectures for the base transfer learned neural network (TL-NN)s are displayed in Fig. 5. Both the TL-NN-A (Fig. 5(a)) and TL-NN-B (Fig. 5(b)) show similar complexity. The TL-NN-A includes one more LSTM layer and the TL-NN-B reduces the dimension in the last LSTM layer to match the final output.

In this work, we employ a TL approach to leverage the knowledge gained from the source domain for the target domain. Specifically, we utilize a fine-tuning strategy with a reduced learning rate, which is a type of parameter-based TL. The parameter-based TL approach belongs to the broader category of model-based TL, which in turn is a sub-category of domain adaptation TL [44]. Given that our source and target domains are different while the task remains the same, parameter-based TL is optimal for our problem. Within parameter-based TL, the two primary options are partial freezing and fine-tuning. We choose fine-tuning because it allows for adjustments throughout the network, which can lead to improved performance. This approach has also been successfully employed in other studies, such as those by Yao and Han [14] and Zhou et al. [15], where fine-tuning yielded positive results. The rationale behind this hierarchical TL strategy is that the source and target domains are highly similar. Both datasets are obtained from battery cells with a similar chemistry (NCA-graphite vs. NMC-silicone/graphite), and the input and output data, as well as the underlying patterns, are analogous across the two domains. Prior literature has shown the effectiveness of TL techniques in such scenarios [15,17–20]. By employing the fine-tuning approach with a reduced learning rate, we can capitalize on the similarities between the source and target domains, while minimizing the need for extensive retraining or architectural changes. This TL strategy allows the model to effectively leverage the knowledge gained from the source domain to improve the performance on the target task, which is crucial for the practical deployment of the proposed approach. The fine-tuning process runs for a maximum of 1000 epochs with a learning rate of 1×10^{-5} and the early stopping criterion being 20 consecutive epochs without a decrease in the validation loss. A detailed overview, including the final performed epochs during fine-tuning, can be found in the Appendix A, Table A.7.

As can be seen in Fig. 2 the output of the TL models are later fed into an optimization model (TL-NN-A) or directly into equations (TL-NN-B) to calculate the DMs. The OCV curve from TL-NN-A is optimized via OCP fitting and the optimization problem defined in Eq. (11). The same procedure, as for generating the ground-truth labels of the experimental data, is followed for OCV fitting: In the first iteration for one cell, the pristine, ideal alignment parameters $\vartheta_{\mathrm{ini}} = [1.02, 1.14, -0.04, -0.14]$ are set as the initial value with the upper and lower boundary being $0.8 \cdot \vartheta_{\mathrm{ini}} \le \vartheta_1 \le 1.1 \cdot \vartheta_{\mathrm{ini}}$. Every succeeding iteration/checkup assumes the prior solution as the initial value and allows the same variation as in the initial run. Because TL-NN-B directly estimates the alignment parameter set ϑ, Eqs. (4) to (7) are enough to calculate the OCV curve and the DMs.

4. Results and discussion

This work investigates the advantages of combining synthetic data with ML and the mechanistic model approach. Especially, the undergone study answers the question about which coupling is the most beneficial for accurate SOH, DM and OCV curve estimation from partial charging voltage segments. Guidelines for the mandatory experiments required to fine-tune pre-trained NNs are derived by defining varying UCs with reduced experimental fine-tuning data for the prior TL models, as shown in Fig. 4.

4.1. Benchmark

Table 5 offers an overview of the models' performance for the respective complete test data, regarding to Fig. 4. From Table 5 it can be seen at first glance that both TL models perform with comparable accuracy. The computationally less complex TL-NN-B, however, performs slightly better, especially in terms of DM accuracy.

4.1.1. Use case 1

Both models achieve high accuracy for UC1A: The $\mathrm{MAE}_{\mathrm{OCV}}$ stays below 8 mV and the $\mathrm{MAPE}_{\mathrm{SOH}}$ below 1.2 %. While LLI is also estimated with high accuracy, the $\mathrm{LAM}_{\mathrm{NE}}$ shows MAEs up to 2.48 % for the

Table 5

Performance comparison of TL-NN-A and TL-NN-B for different UCs and their complete test data. The UCs differ in the amount of training data for the training/fine-tuning process.

		$\mathrm{MAPE}_{\mathrm{SOH}}$	$\mathrm{MAE}_{\mathrm{OCV}}$	$\mathrm{MAE}_{\mathrm{LAM\text{-}NE}}$	$\mathrm{MAE}_{\mathrm{LAM\text{-}PE}}$	$\mathrm{MAE}_{\mathrm{LLI}}$
UC1A	TL-NN-A	1.16 %	7.55 mV	2.48 %	2.13 %	0.82 %
	TL-NN-B	0.96 %	5.83 mV	0.97 %	0.73 %	0.81 %
UC1B	TL-NN-A	3.67 %	15.8 mV	2.57 %	3.81 %	2.80 %
	TL-NN-B	2.62 %	14.0 mV	2.41 %	1.17 %	2.36 %
UC2A	TL-NN-A	1.17 %	8.21 mV	2.83 %	2.03 %	0.97 %
	TL-NN-B	1.21 %	7.23 mV	1.40 %	0.61 %	1.11 %
UC2B	TL-NN-A	4.06 %	19.2 mV	3.22 %	3.71 %	3.43 %
	TL-NN-B	3.13 %	18.8 mV	2.99 %	1.55 %	3.29 %
UC3A	TL-NN-A	1.86 %	10.2 mV	2.97 %	2.27 %	1.21 %
	TL-NN-B	1.54 %	12.4 mV	1.28 %	1.26 %	1.27 %
UC3B	TL-NN-A	5.00 %	31.9 mV	5.49 %	3.78 %	5.24 %
	TL-NN-B	4.97 %	32.7 mV	5.06 %	4.18 %	4.16 %

TL-NN-A model. Due to less fine-tuning data in UC1B, the performance worsens for both models and the $\mathrm{MAE}_{\mathrm{OCV}}$ rises above 15 mV. Obviously, due to a lower $\mathrm{LAM}_{\mathrm{PE}}$ estimation accuracy, also the $\mathrm{MAPE}_{\mathrm{SOH}}$ is worse for TL-NN-A. Fig. 6 and Fig. B.14 (in Appendix B.1) offer a more detailed analysis in regards to varying input voltage windows. Interestingly, both models barely show any voltage-window-dependency. There is a slight tendency towards lower voltage segments, as discussed in our previous work [17]: Cells with graphite anodes show the highest gradient of their OCP during the begin of charge of the full cell, as can be seen in Fig. 1(a). This gradient is detectable in the full cell voltage response during constant-current charging and, hence, allows to estimate the anode degradation. On the other side, upper voltage segments only include one detectable change of gradient due to the anode. In some cases this is not only difficult to distinguish from the cathodic gradient changes but further does not include as much information as the gradient changes in the lower voltage segment. Even with very limited input data, i.e., a partial charging curve from 3.8 V to 4.0 V, the $\mathrm{MAE}_{\mathrm{OCV}}$ stays below 10 mV and the DMs are estimated with adequate accuracy. This behavior drastically changes for UC1B: With limited fine-tuning data, the voltage-window-dependency increases. While segments from the lower range still achieve comparable results to UC1A, both models have resulting $\mathrm{MAE}_{\mathrm{OCV}}$ above 30 mV for a lower cutoff voltage of 3.8 V, i.e., $V_{\mathrm{min}} \geq 3.8\,\mathrm{V}$. Fig. B.14 in Appendix B.1 shows that TL-NN-A has more stable estimations and shows higher interpretability. This can also be attributed to the fact that TL-NN-A is not designed to directly produce the alignment parameters and, consequently, the DMs. TL-NN-B, however, seems to already include overfitted sections, i.e., voltage windows with a lower cutoff voltage of 3.6 V. The observation that nearly every estimated variable from these limited voltage windows surpasses the accuracy of those estimated with the full input voltage window suggests an increased likelihood of overfitting. The full voltage window encompasses more information than the partial segments and should, therefore, be capable of achieving higher estimation accuracy compared to any individual partial voltage window. Moreover, TL-NN-B reaches low $\mathrm{LAM}_{\mathrm{PE}}$ errors, independent of the input data, leading to the same assumption. Figs. 7 and 8 display the reduction of the input data to only one sample at a specific SOH and with input data from the C/2 charging events for UC1A. Fig. 7, specifically, visualizes the measured and estimated OCV, ICA and DVA for samples at a SOH of 91 %. The OCV trajectory (Fig. 7(a), (d), (g), (j)) shows that all models underestimate the SOH. However, a more detailed analysis can be derived from the ICA (Fig. 7 (b), (e), (h), (k)) and DVA (Fig. 7(c), (f), (i), (l)). The prior TCN-LSTM model introduces high noise in the reconstructed signal, evident in several peaks. Despite this, the mean peaks and valleys caused by electrode degradation are accurately captured. The optimized models TL-NN-A and TL-NN-B align well with the positions of all peaks and valleys, though the peaks appear exaggerated and sharper compared to real measurements. This discrepancy is due to the impedance rise and increasing inhomogeneity in the real cell, causing the extrema in the ICA and DVA to diminish slightly [59]. The reconstructed signals fail to account for this behavior accurately because they are calculated from pristine OCP measurements. This behavior becomes clearer when comparing with Figs. B.12 and B.13 in Appendix B.1. At the pristine state, the amplitude of all peaks in the ICA matches for both TL-NN-A and TL-NN-B. For the aged cell with a SOH of 81 % (Fig. B.13), the measured peaks decrease in amplitude, and the mismatch between measured and reconstructed signals increases.

Since directly comparing the model output (OCV) with the measured voltage curve using Figs. 7, B.12, and B.13 is challenging, we evaluate the error trajectory for all analyzed input data, summarized in Fig. 8. It shows the error course of the estimated OCV from the prior TCN-LSTM network within TL-NN-A and the final OCV reconstructions error from TL-NN-A and TL-NN-B. This evaluation is presented for three distinct aging states SOH = 100 %, SOH = 91 % and SOH = 84 % and four varying SOC ranges: low range from approximately 0 % to 50 %, the mid range from approximately 20 % to 90 %, the high range from approximately 50 % to 100 % and the full range. Note that the input segments are snipped based on voltage boundaries, as described in Fig. 8, hence, the SOC ranges are rough estimates. As before, the evaluation shows both models perform with high accuracy and that the error mostly stays within the 20 mV boundaries. Even the first estimate from the stand-alone TCN-LSTM model in path A achieves satisfactory results. These estimations, however, still include noisy artifacts, as visible when comparing all three lines. Reconstructing the OCV via optimization not only allows the estimation of the DMs but also the correction of the OCV curve. Although the $\mathrm{MAE}_{\mathrm{OCV}}$ barely reduces with optimization, the final results are more realistic and represent the physico-chemical effects of battery aging. In general, the reconstruction accuracy slightly decreases for higher degradation, as can be seen in Fig. 8. This is reasonable due to the increasing internal resistance leading to higher overpotentials and, hence, less visible features of the OCPs in the full cell voltage trajectory. Interestingly, the general course of the error course seems similar for one C/2 measurement at the same SOH with varying input voltage segments. The offset to zero, however, decreases for the full input segment. The models seem to interpret similar features of the input data, independent of the voltage segment. For all samples and models especially the error below 1 Ah has a dynamic trajectory due to the high gradient in the lower SOC region in combination with many gradient changes. Non-accurate estimations of the shifting between both OCPs, thus, generate this special trend. For each sample, an increasing OCV error is observed towards the end of the charge cycle. This phenomenon can be attributed to the model's imperfect estimation of the SOH, leading to a premature termination of either the reconstructed or the measured OCV. During this phase, the OCV rises rapidly, as illustrated in Fig. 1(a), thereby causing a substantial increase in the error. An unusual behavior is the negative error in the beginning of the reconstruction for the plain TCN-LSTM

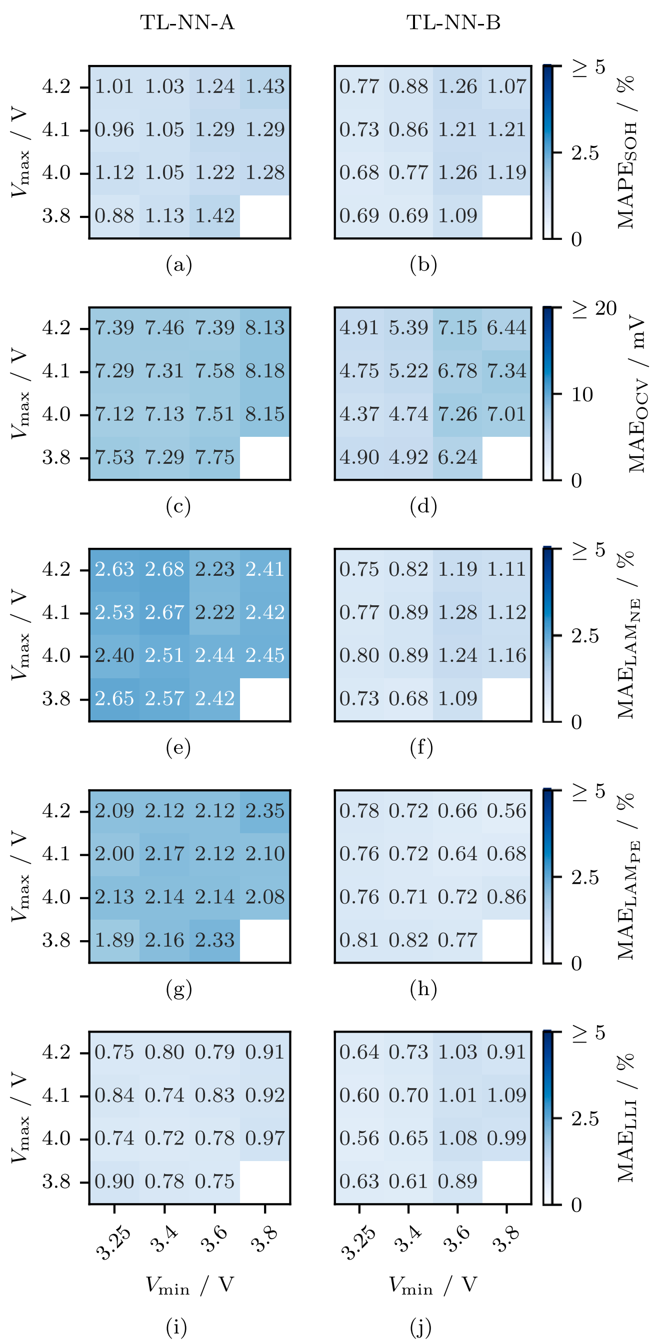

Fig. 6. SOH estimation, DM estimation and OCV reconstruction accuracy for model TL-NN-A and TL-NN-B for UC1A and varying partial voltage input charging curves. The Subfigures show in detail the $\mathrm{MAPE}_{\mathrm{SOH}}$ for (a) TL-NN-A and (b) TL-NN-B, the $\mathrm{MAE}_{\mathrm{OCV}}$ for (c) TL-NN-A and (d) TL-NN-B, the $\mathrm{MAE}_{\mathrm{LAM\text{-}NE}}$ for (e) TL-NN-A and (f) TL-NN-B, the $\mathrm{MAE}_{\mathrm{LAM\text{-}PE}}$ for (g) TL-NN-A and (h) TL-NN-B, and the $\mathrm{MAE}_{\mathrm{LLI}}$ for (i) TL-NN-A and (j) TL-NN-B.

model and the samples from 100 % SOH. The NN overestimates the OCV curve by up to 20 mV, independent of the input voltage segment. This behavior can be explained by an overestimation of $\mathrm{LAM}_{\mathrm{NE}}$. The OCV error reaches even −50 mV for end of charge which simply is due to an earlier cutoff and a lower estimated SOH.

4.1.2. Use case 2

We conduct the same analysis for UC2A and UC2B in Figs. 9 and B.15, Appendix B.2, with a similar result: Both approaches work excellent for UC2A, but struggle to achieve comparable performance for UC2B, which is also supported by Table 5. While the $\mathrm{MAE}_{\mathrm{OCV}}$ still remains below 10 mV, the $\mathrm{MAPE}_{\mathrm{SOH}}$ below 2 % and all DMs mostly below 3 % for UC2A, this behavior changes for UC2B: The TL-NN-A reaches similar results only for the lower and full SOC ranges with a lower cutoff voltage below 3.4 V. The TL-NN-B even requires a start SOC of 0 % to maintain similar accuracy. The overall performance is highly influenced by the input data and a lower cutoff voltage generally leads to higher accuracy. As in UC1B, there seems to be an overfitted section with input data and a lower cutoff voltage of 3.6 V for TL-NN-B.

4.1.3. Use case 3

As listed in Table 5 both models perform comparably well for UC3A with an OCV reconstruction error below 13 mV and a $\mathrm{MAPE}_{\mathrm{SOH}}$ below 2 %. Interestingly, TL-NN-B shows higher estimation accuracy in terms of SOH and DMs while the OCV reconstruction error is higher. The UC3B, however, seems to mark the boundary of successful TL because for both models the OCV reconstruction error exceeds 30 mV and all states are estimated with unusable accuracy. Figs. 10 and B.16, Appendix B.3, compare both models and UCs according to varying input voltage windows. The voltage-window-dependency is strongly visible for both models in UC3A, Fig. 10. Both models achieve adequate reconstruction and estimation accuracy for voltage windows with $V_{\min} \leq 3.6\,\mathrm{V}$. TL-NN-A struggles to maintain high accuracy for $\mathrm{LAM}_{\mathrm{NE}}$ estimation, whereas TL-NN-B maintains a MAE below 2 % for all input windows. This behavior drastically changes for UC3B: Both models fail to apply their transferred knowledge and the OCV reconstruction error stays above 25 mV for all input data. Fig. B.16 in Appendix B.3 reveals that both models fail to estimate the anode aging which of course leads to worsened OCV reconstruction and, hence, less accurate loss of lithium inventory (LLI) and SOH estimation. For TL-NN-A, however, the voltage-window-dependency is still very visible, especially for the SOH and $\mathrm{LAM}_{\mathrm{PE}}$ estimation. Fig. 11 presents the estimation accuracy per aging path from the test data for UC3A and TL-NN-A. UC3A offers the most challenging and still successful TL step with very limited fine-tuning data from cells which do not show the complete degradation, as can be seen in Fig. 3 and Table 1. According to the findings from our previous study [17] and the included information from Table 1 we expect TL-NN-A to not reach high accuracy for samples with SOH ≤ 85 %, $\mathrm{LAM}_{\mathrm{NE}} \geq 15\,\%$, $\mathrm{LAM}_{\mathrm{PE}} \geq 8\,\%$ or LLI ≥ 15 %. In Fig. 11, however, this theory cannot be confirmed completely. For the degradation paths with lower degradation, i.e., path C (Cycling (3.6 V – 4.2 V)) and path E (Storage (3.7 V)), the model performs well besides a small overestimation of $\mathrm{LAM}_{\mathrm{PE}}$. The standard deviation remains narrow and especially LLI and SOH are estimated with high accuracy. Even for the two degradation paths with higher degradation, i.e., path A (Cycling (2.5 V – 4.2 V)) and path D (Cycling (WLTP)), the accuracy stays high for the LLI and SOH estimation. Again, $\mathrm{LAM}_{\mathrm{PE}}$ is overestimated for all checkups but the standard deviation stays narrow until the last checkups. During the state of higher degradation, the TL-NN-A loses accuracy, estimations get worse and standard deviation increases. This trend, however, does not start once $\mathrm{LAM}_{\mathrm{PE}} \geq 8\,\%$, but rather once $\mathrm{LAM}_{\mathrm{PE}} \geq 15\,\%$. The $\mathrm{LAM}_{\mathrm{NE}}$ estimations also start to show wide standard deviations ranging from 0 % to 25 % once the measured $\mathrm{LAM}_{\mathrm{NE}}$ exceeds approximately 15 %. This is again in well agreement with the prior assumption [17].

In Table 5 the MAE for $\mathrm{LAM}_{\mathrm{NE}}$ and $\mathrm{LAM}_{\mathrm{PE}}$ stays below 3 % for TL-NN-A. Comparing with Fig. 11 this seems inconsistent because estimation for aging path A (Cycling (2.5 V–4.2 V)) and D (Cycling (WLTP)) gets highly inaccurate with absolute deviations up to 20 %. This high variance can be either be interpreted as low confidence estimation or as some samples with high deviations in relation to the full dataset performance. The final scalar metric is calculated from the entire test dataset. The influence of outliers in the dataset is diminished due to the large data size. Therefore, it is highly recommended to not solely rely on a single metric, but rather analyze individual samples and smaller

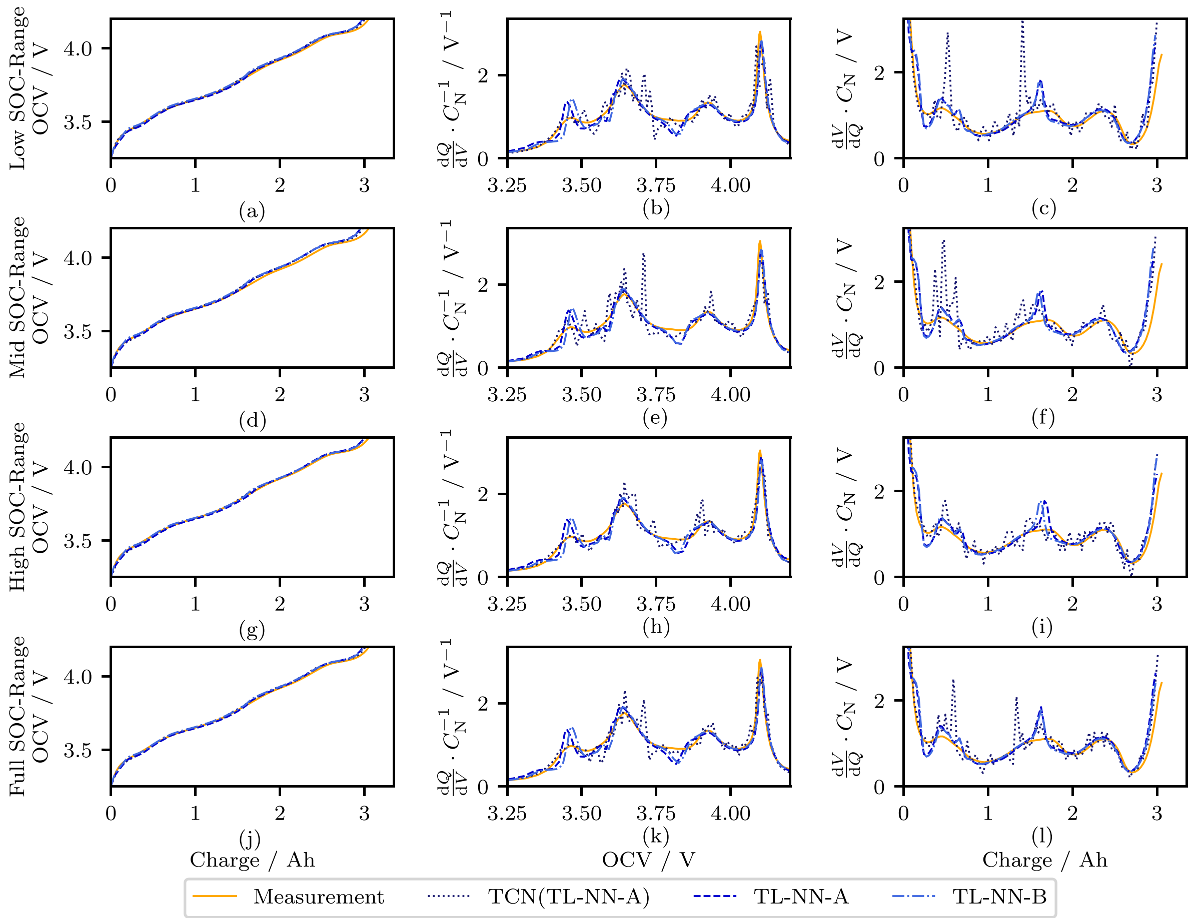

Fig. 7. Evaluation of the OCV, ICA and DVA reconstruction from the prior TCN-LSTM model from TL-NN-A, the final TL-NN-A and TL-NN-B, which includes the performance for UC1A and test data drawn from partial charging events at C/2 and a SOH of 91 %. Four different voltage / SOC windows are evaluated: The low SOC-range ((a)–(c)) corresponds to a voltage window from 3.25 V to 3.8 V, the middle window ((d)–(f)) from 3.6 V to 4.1 V and the high SOC-range ((g)–(i)) from 3.8 V to 4.2 V. Subfigures (j)–(l) show the results for the full input voltage.

subsets of the test dataset to identify high variance in the model's estimation performance.

4.2. Comprehensive discussion

The results of our study reveal the benefits of coupling simulation data with ML and the mechanistic model approach. Both models prove their applicability for OCV reconstruction and DM estimation, even for limited fine-tuning data. During the A UCs, fine-tuning data is limited even further but it includes samples from every C-rate. This allows the TL-NN-A and TL-NN-B to maintain high accuracy independent of the input voltage window. All B UCs aggravate the TL by eliminating some C-rates from the fine-tuning data. This leads to stronger requirements for the input voltage window, i.e., lower cutoff voltage, for UC1B and UC2B. For UC3B, however, an accurate reconstruction is not possible anymore because the fine-tung data only includes samples from C/2. Both models, TL-NN-A and TL-NN-B, perform comparably well. As can be seen in Table 5, TL-NN-B reaches lower DM estimation errors. Besides that, TL-NN-B convinces by reduced computational requirements: The initial output from the TL-NN-B only includes four scalars (Fig. 5(b)) and the OCV curve can be calculated with a simple equation, see Eq. (2). The coupling of TL with optimization, however, yields more interpretable results with more stable estimation and a stronger voltage-window-dependency, e.g., compare with Fig. B.14 in Appendix B.1 and B.15 in Appendix B.2. The TL-NN-A does not show any obvious overfitted section and yields reasonable $\mathrm{LAM}_{\mathrm{NE}}$ errors for the upper voltage segments.

As can be seen in Fig. 5(a) the TL-NN-A model deviates from the tuned architecture in our previous work [17], i.e., the model is more complex and includes two additional LSTM-layers. The input TCN layer, however, has almost the same hyperparameters which is a result of the similar training data. The higher complexity can be explained by the extended data including more C-rates and voltage windows. The number of epochs increases for higher UCs which may be due to a challenging training dataset in the lower UCs: The models get eventually stuck in a local optimum early in the fitting process. For sparse data the optimization landscape may be more well-defined and the fitting process is likely to run into overfitting. On the other hand, the diverse experimental data in the early UCs works as a type of regularization and prevents the models from overfitting [60]. In our previous work [17], we have shown with our UCs that fine-tuning with data from multiple cells but only at one C-rate leads to worsened performance with OCV reconstruction errors around 20 mV for varying voltage windows. This extended study at hand reveals that also the implicit DMs play a crucial role. By selecting fine-tuning data from the cells which show the highest degradation, i.e., from path A (Cycling (2.5 V – 4.2 V), compare Table 1), and including all C-rates we optimize the performance of both models and consequently reach OCV reconstruction errors below 10 mV independent of the input data. Although the model developed in our prior study [17] was fine-tuned with two cells from varying aging

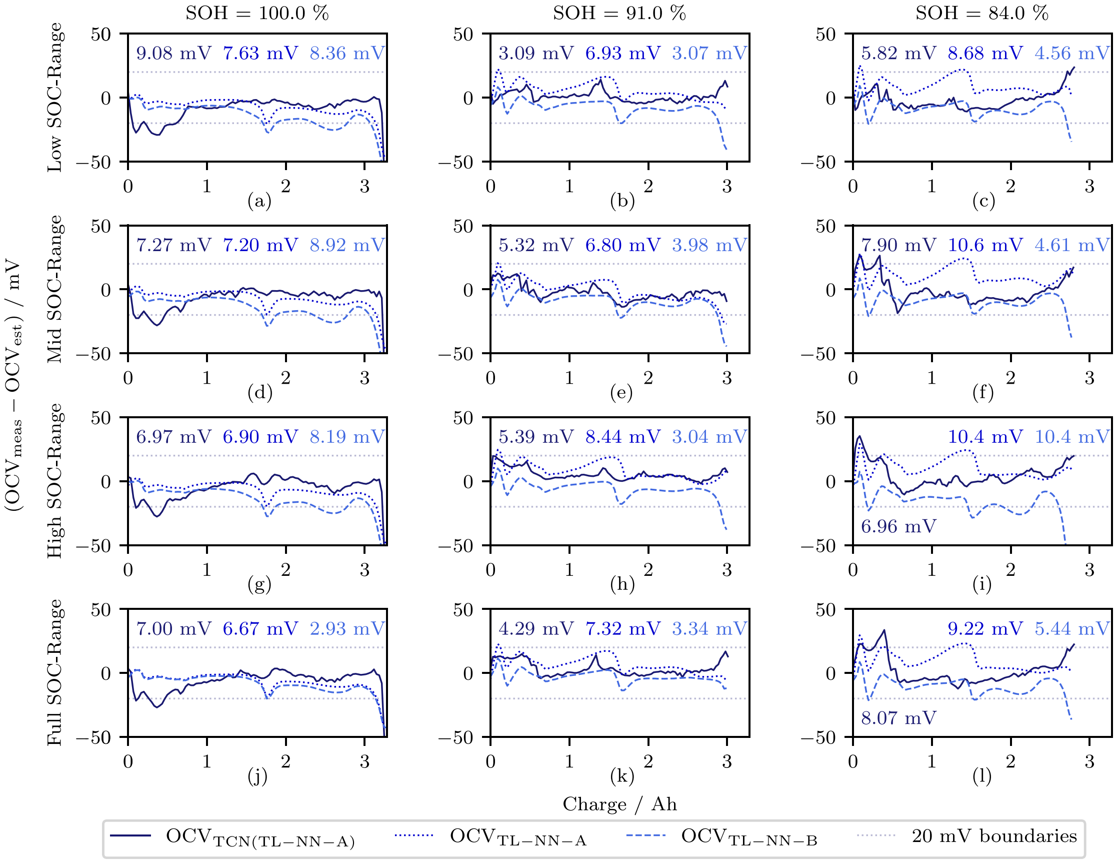

Fig. 8. Evaluation of the OCV reconstruction error from the prior TCN-LSTM model from TL-NN-A, the final TL-NN-A and TL-NN-B, which includes the performance for UC1A and test data drawn from partial charging events at C/2. The error course is plotted over the charge throughput of the OCV measurement during the respective checkup. Three degradation states and four different voltage / SOC windows are evaluated: The low SOC-range ((a)–(c)) corresponds to a voltage window from 3.25 V to 3.8 V, the middle window ((d)–(f)) from 3.6 V to 4.1 V and the high SOC-range ((g)–(i)) from 3.8 V to 4.2 V. Subfigures (j)–(l) show the results for the full input voltage. The 20 mV error boundaries are plotted for better visibility in dashed gray lines. For all evaluated scenarios the MAE$_{OCV}$ error is included in the subplot, in its respective color. The left text belongs to the prior TCN-LSTM from TL-NN-A, the middle text to the final TL-NN-A, while the right text corresponds to the TL-NN-B.

paths and, hence, the learned degradation pattern is more diverse, the error is above 10 mV for any input data segment with a lower cutoff voltage $V_{min} \geq 3.4$ V. Comparing both studies, we can conclude that this behavior must be due to the included samples at C/2 in the fine-tuning of TL-NN-A and TL-NN-B. In contrast to our previous study [17], by introducing an alternative UC definition, according to Fig. 4, we have revealed that extrapolation of estimation is possible to some extent. For UC3A the TL-NN-A is able to estimate the correct DMs and SOH for two degradation paths which show higher DMs than the fine-tuning data. The standard deviations for the LAM estimations, however, increase once the input samples move too far away from the re-learned fine-tuning data. On the other hand, this extrapolation is not possible in combination with varying C-rates as in UC3B: The model cannot conclude the correct OCV just from fine-tuning with data at the medium C-rate and medium degradation.

Comparing our work to a purely optimization-based approach as in the work by Schmitt et al. [28], we can reach more accurate DM estimations even for partial charging events at higher C-rates. Schmitt et al. [28] concluded that at least a C-rate below C/15 or partial charging segments spanning at least the SOC range from 20 % to 70 % at an even lower C-rate of C/30 are necessary to yield accurate DM estimations. Especially for the upper voltage segments our approach outperforms the model by Schmitt et al. [28] in terms of DM estimation accuracy: For a partial voltage segment, measured at C/30 from 50 % to 85 % SOC, Schmitt et al. [28] have reached a RMSE$_{\text{LAM-NE}}$ of 14.4 %, a RMSE$_{\text{LAM-PE}}$ of 2.5 % and a RMSE$_{\text{LLI}}$ of 8.3 %. This SOC range approximates to the voltage window from 3.8 V to 4.1 V independent of the applied C-rate. For all of the UCs UC1A, UC2A and UC3A both models – TL-NN-A and TL-NN-B – maintain DM estimation MAEs below 3 % (RMSE$_{\text{LAM-NE}} \leq 5.08$ %, RMSE$_{\text{LAM-PE}} \leq 3.67$ %, RMSE$_{\text{LLI}} \leq 1.95$ %) even for a test data comprising of voltage curves solely captured at an applied current between C/3.85 and 1C (compare Figs. 6, 9 and 10). A similar improvement holds true for the OCV reconstruction and SOH estimation error: While Schmitt et al. [28] reached a RMSE$_{\text{OCV}}$ of 32 mV and RMSE$_{\text{SOH}}$ of 8.0 % our TL-NN-A maintains a MAE$_{\text{OCV}}$ below 12.2 mV (RMSE$_{\text{OCV}} \leq 14.4$ mV) and a MAPE$_{\text{SOH}}$ below 2.47 % (RMSE$_{\text{SOH}} \leq 2.46$ %) for the A UCs. Similar, the TL-NN-B yields a MAE$_{\text{OCV}}$ below 18.1 mV (RMSE$_{\text{OCV}} \leq 24.2$ mV) and a MAPE$_{\text{SOH}}$ below 1.63 % (RMSE$_{\text{SOH}} \leq 1.77$ %). While this example is only on selected voltage window, the general trend holds true for all input voltage segments and even applies for the lower voltage segments from UC1B and UC2B (compare Figs. 6, B.14 in Appendix B.1, 9, B.15 in Appendix B.2, 10, B.16 in Appendix B.3).

The comparison with the developed TCN network by Bockrath et al. [8], which directly estimates the SOH from partial discharge voltage segments at approximately C/2, allows to evaluate the benefit of the TL step from synthetic data: Their developed NN reaches a RMSE$_{\text{SOH}}$ of 1.0 % for 3.2 V to 4.2 V, 13.1 % for 3.2 V to 3.5 V, 2.9 % for 3.5 V to 3.7 V and 1.4 % for 3.7 V to 4.2 V [8]. These values lie in a comparable range to our MAPE$_{\text{SOH}}$ for varying UCs and both models TL-NN-A and TL-NN-B (compare Fig. 6, B.14 in Appendix B.1, 9, B.15 in Appendix B.2, 10, B.16 in Appendix B.3). Contrary to our thesis, they concluded

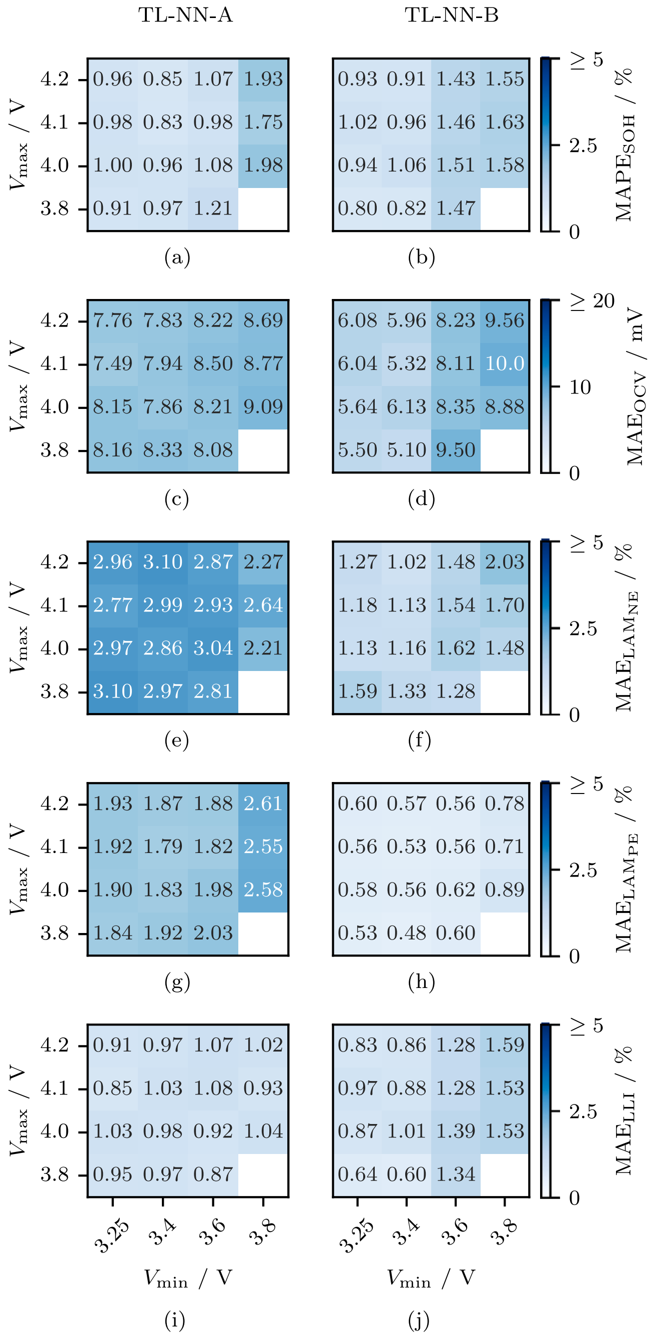

Fig. 9. SOH estimation, DM estimation and OCV reconstruction accuracy for model TL-NN-A and TL-NN-B for UC2A and varying partial voltage input charging curves. The Subfigures show in detail the $\mathrm{MAPE_{SOH}}$ for (a) TL-NN-A and (b) TL-NN-B, the $\mathrm{MAE_{OCV}}$ for (c) TL-NN-A and (d) TL-NN-B, the $\mathrm{MAE_{LAM\text{-}NE}}$ for (e) TL-NN-A and (f) TL-NN-B, the $\mathrm{MAE_{LAM\text{-}PE}}$ for (g) TL-NN-A and (h) TL-NN-B, and the $\mathrm{MAE_{LLI}}$ for (i) TL-NN-A and (j) TL-NN-B.

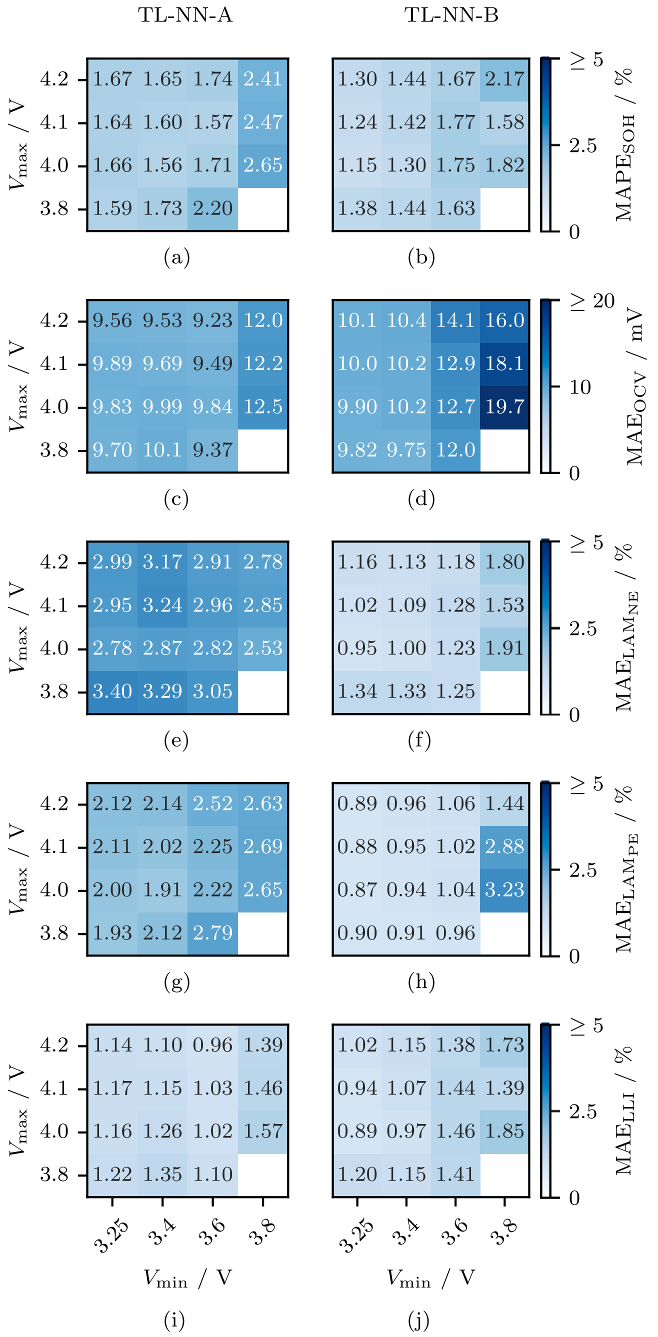

Fig. 10. SOH estimation, DM estimation and OCV reconstruction accuracy for model TL-NN-A and TL-NN-B for UC3A and varying partial voltage input charging curves. The Subfigures show in detail the $\mathrm{MAPE_{SOH}}$ for (a) TL-NN-A and (b) TL-NN-B, the $\mathrm{MAE_{OCV}}$ for (c) TL-NN-A and (d) TL-NN-B, the $\mathrm{MAE_{LAM\text{-}NE}}$ for (e) TL-NN-A and (f) TL-NN-B, the $\mathrm{MAE_{LAM\text{-}PE}}$ for (g) TL-NN-A and (h) TL-NN-B, and the $\mathrm{MAE_{LLI}}$ for (i) TL-NN-A and (j) TL-NN-B.

that the upper voltage segments are better suitable for SOH estimation due to higher correlation between the accumulated charge in this segments and the full capacity throughput. When it comes to OCV reconstruction and DM estimation, however, our findings show that the lower voltage segments are better suited, which also aligns with the results from Schmitt et al. [28]. In essence, this phenomenon can be attributed to the geometrical characteristics, specifically the gradient variations within the voltage curve. Capturing and learning a greater number of these features across the potential degradation range of a battery cell enhances the accuracy of OCV reconstruction and SOH estimation. Ultimately, minimal electrochemical knowledge but rather mathematical understanding is required to develop data-driven models that effectively learn the trends of battery degradation.

The only comparable study to evaluate the coupling of ML and the mechanistic model approach was derived by Tian et al. [25]: They have trained a NN to estimate the stoichiometries from partial charging voltage segments at 1C and directly derived the OCV curve from that. For 200 mV voltage segments at varying SOC positions their reconstructed OCV curve maintained RMSEs below 15 mV and the derived $\mathrm{MAE_{SOH}}$ was under 3.7 %. Their estimated DMs accuracies were not

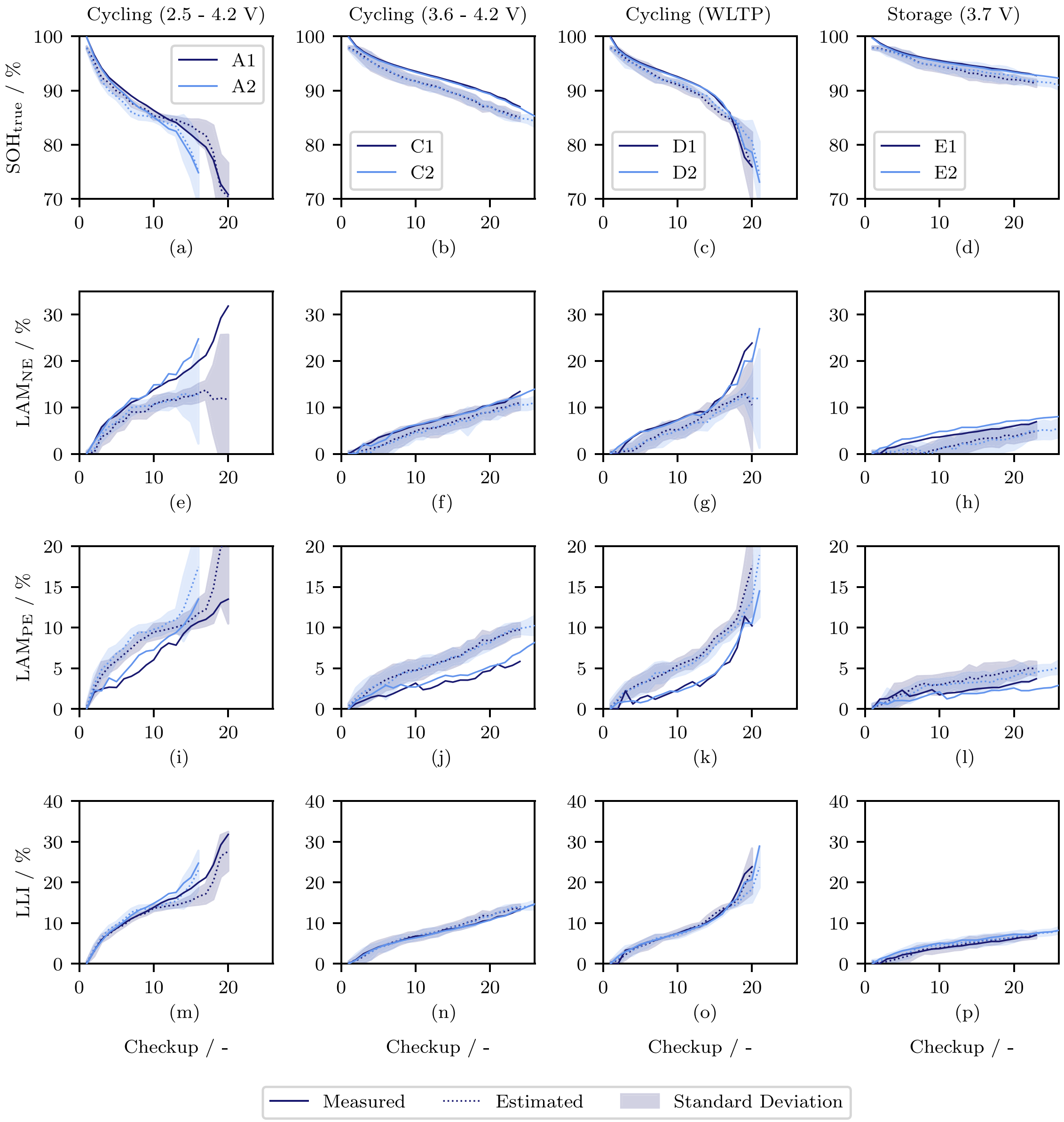

Fig. 11. Measured and estimated SOH and DMs for UC3A and TL-NN-A. The true values are displayed in solid lines, while the estimations from both cells per aging path are pointed with the shaded areas showing the standard deviation. The standard deviation shows the result of all estimations at one aging state with all different possible voltage windows.

fully specified but – visually analyzed – stayed in good agreement with their reference. Their LAM$_{\text{NE}}$ estimation, however, starts to increase its deviation for later cycles. Our developed TL-NN-B follows a very similar approach but includes TL to aggravate more training data, which seems to benefit the OCV reconstruction. For 200 mV input segments the TL-NN-B reconstructs the OCV curve for UC1A and UC2A with a MAE below 9.5 mV (RMSE$_{\text{OCV}}$ ≤ 16.1 mV) and also the MAPE$_{\text{SOH}}$ stays under 1.58 % (MAE$_{\text{SOH}}$ ≤ 1.46 %, compare Figs. 6, 9).

As in any data-driven method, our results show that training data – source and target domain – heavily influence the performance. Previous findings [17] already prove the eligibility of synthetic data as the source domain and prove that the source domain must cover all possible variations in terms of C-rate, SOC window or DMs of the target domain. Additionally, our previous study [17] highlights that the choice and amount of synthetic data for pretraining do not matter as long as it includes a sufficient amount of supporting points within the boundaries of the describing parameters, ensuring accurate representation within the target domain. Due to our UC definition in Fig. 4 we can conclude that also the fine-tuning data from the target domain highly matters: To allow accurate OCV reconstruction it must at least include the boundaries of the test data, as can be seen in Table 5. This implies that the fine-tuning data should always be selected from the cells showing the highest degradation. Further, the lowest and highest C-rates of all samples, i.e., C/3.85 and 1C as in our UC3A, must be included as well. It remains an open research question to determine the extent to which this simplification of fine-tuning data can be pursued in real-world scenarios including battery cell validation in industry application. On one hand, it is crucial to understand the validity of this assumption across varying dataset sizes. On the other hand, research must be conducted to explore how much the fine-tuning data can be minimized to ascertain whether highly accelerated aging tests are sufficient for this purpose. With these findings it will be possible to conclude possible time and cost savings enabled by TL from synthetic data.

The comparison of both model architectures – TL-NN-A coupling TL and optimization, and TL-NN-B coupling TL and the mechanistic model – is challenging to conclude with a clear advantage on one

Table 6

A typical experiment design for aging model parametrization according to industry experience and literature [61]. The used experimental data [28] in our approach is highlighted (lightgray) including the resulting capacity fade and DMs, as well as the reduced fine-tuning data for UC2A (darkgray).

Aging condition	Current profile	Temperature	SOC / Voltage-range	ΔSOH	$\Delta\mathrm{LAM}_{\mathrm{NE}}$	$\Delta\mathrm{LAM}_{\mathrm{PE}}$	ΔLLI
Cyclic	0.5C	25 °C	2.5 V to 4.2 V				
			2.5 V to 4.0 V				
			3.6 V to 4.2 V				
		35 °C	2.5 V to 4.2 V				
			2.5 V to 4.0 V				
			3.6 V to 4.2 V				
	1C	25 °C	2.5 V to 4.2 V	30 %	30 %	15 %	35 %
			2.5 V to 4.0 V	15 %	15 %	8 %	15 %
			3.6 V to 4.2 V	15 %	15 %	8 %	15 %
		35 °C	2.5 V to 4.2 V				
			2.5 V to 4.0 V				
			3.6 V to 4.2 V				
	WLTP	25 °C		25 %	25 %	15 %	30 %
		35 °C					
	3N3F	10 °C					
		25 °C					
		35 °C					
Calendaric		25 °C	10 %				
			50 %	10 %	8 %	2.5 %	10 %
			100 %				
		50 °C	10 %				
			50 %				
			100 %				

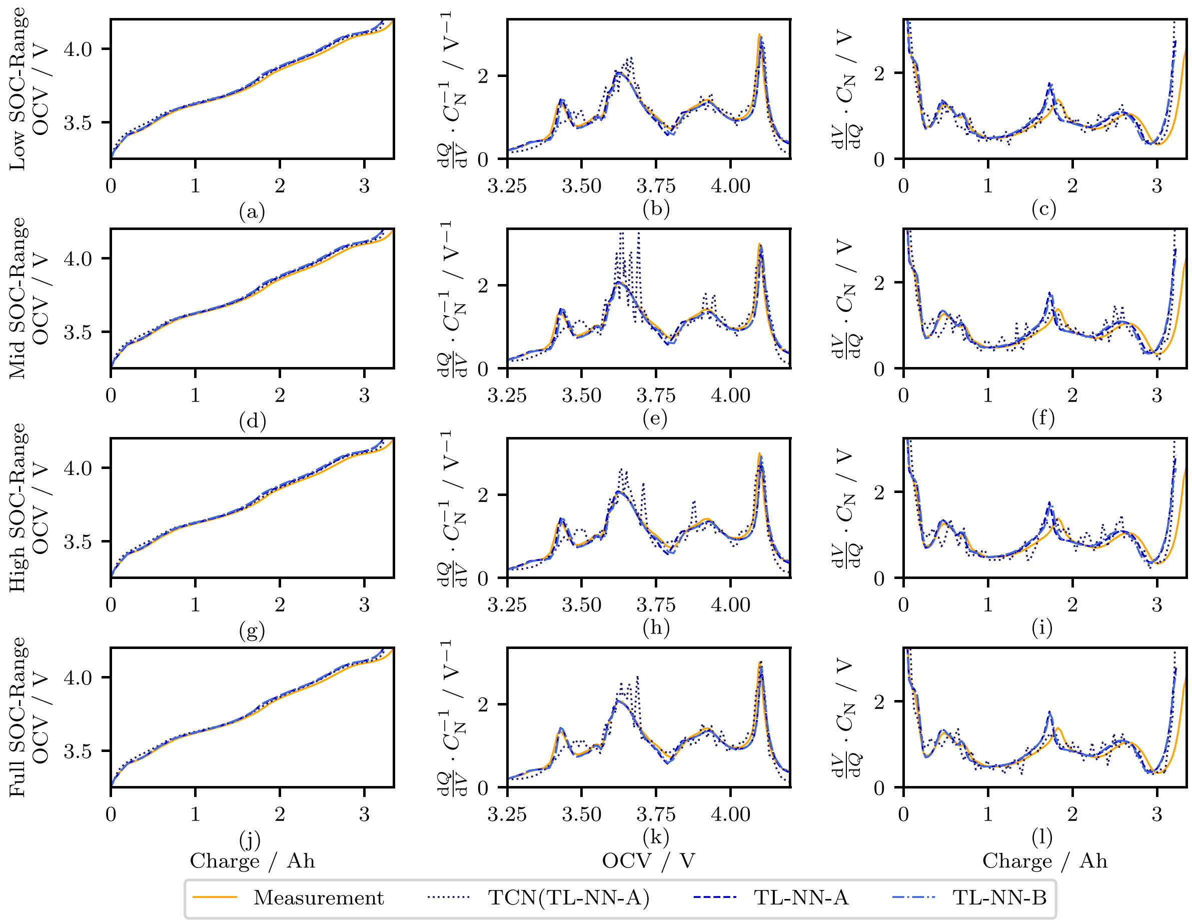

Fig. B.12. Evaluation of the OCV, ICA and DVA reconstruction from the prior TCN-LSTM model from TL-NN-A, the final TL-NN-A and TL-NN-B, which includes the performance for UC1A and test data drawn from partial charging events at C/2 and a SOH of 100 %. Four different voltage / SOC windows are evaluated: The low SOC-range ((a)–(c)) corresponds to a voltage window from 3.25 V to 3.8 V, the middle window ((d)–(f)) from 3.6 V to 4.1 V and the high SOC-range ((g)–(i)) from 3.8 V to 4.2 V. Subfigures (j)–(l) show the results for the full input voltage.

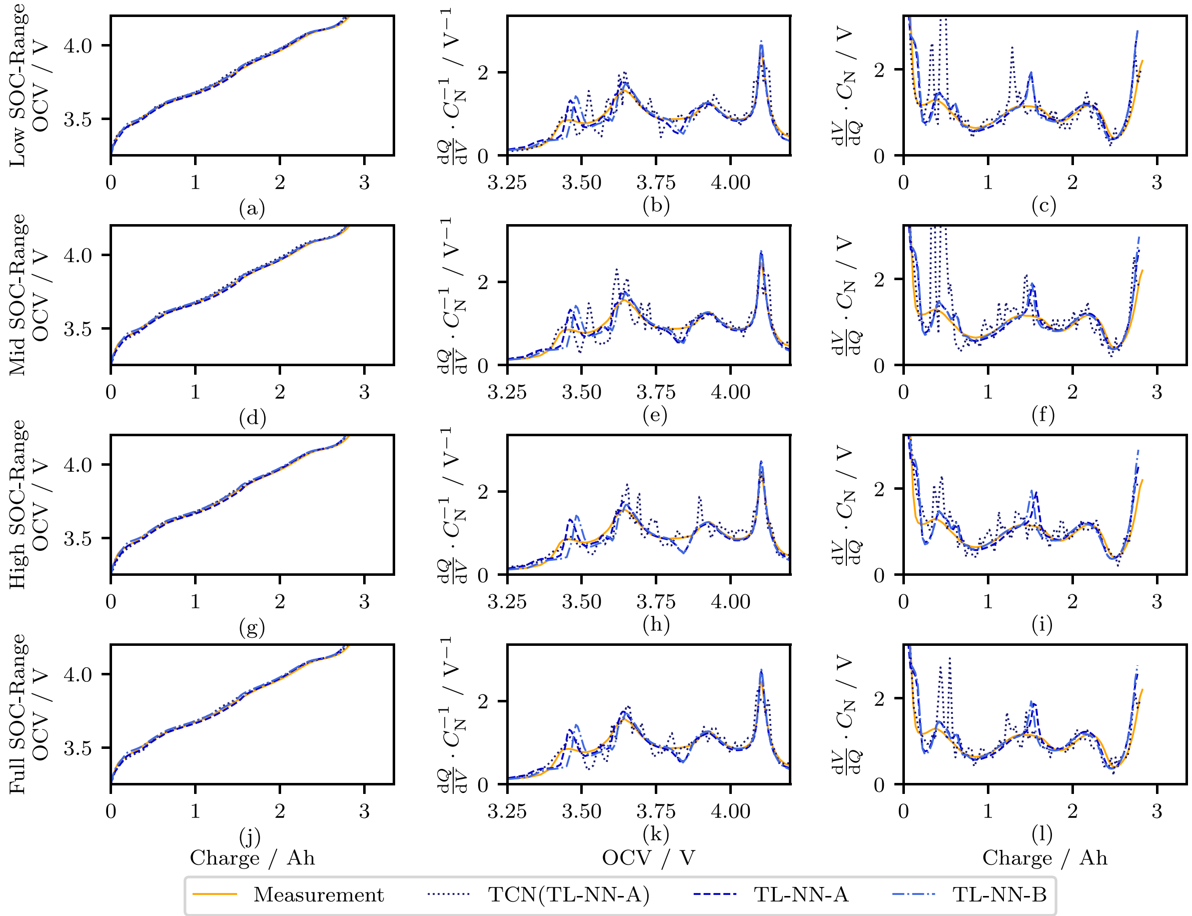

Fig. B.13. Evaluation of the OCV, ICA and DVA reconstruction from the prior TCN-LSTM model from TL-NN-A, the final TL-NN-A and TL-NN-B, which includes the performance for UC1A and test data drawn from partial charging events at C/2 and a SOH of 84 %. Four different voltage / SOC windows are evaluated: The low SOC-range ((a)–(c)) corresponds to a voltage window from 3.25 V to 3.8 V, the middle window ((d)–(f)) from 3.6 V to 4.1 V and the high SOC-range ((g)–(i)) from 3.8 V to 4.2 V. Subfigures (j)–(l) show the results for the full input voltage.

side. The TL-NN-B, however, has less computational complexity and slightly outperforms the TL-NN-A in almost any UC. It has the downside of requiring the exact alignment parameters for both, the source and target domain, for model training. This requirement can often not be fulfilled, whereas the TL-NN-A suffices with the captured OCV and the pristine alignment parameters, without any additional label. Hence, TL-NN-A allows the OCV reconstruction and DM estimation applied to almost any battery aging test.

The results from UC2A show that a huge reduction of the planned experiments is possible if a pretrained TL model is used. Our findings strongly suggest that the exact aging path does not matter as long as the explicit fine-tuning data provoke the highest degradation in terms of SOH and DMs. If we assume that Table 6 is the standard for data-driven aging model parametrization, we reduce the number of required experiments from 23 to 1. If we assume that one aging experiment runs for 500 days, a checkup is performed every 30 days and a climate chamber makes up 36 % of the aging costs (cycling + storage), the TL approach can reduce the costs by 95 %.

Especially TL-NN-A, due to its low requirements on fine-tuning data, offers a high probability of being successfully applied to onboard or backend BEV algorithms. Offering aging-path-individual OCV updates takes a huge step towards optimized battery usage strategy, increases the accuracy of state estimation and eventually prolongs the lifetime. The gathered knowledge from this study enables the refinement of typical experiment designs for their validity in advance. Many planned measurements can be pre-analyzed to determine their location in the source or target domain. Ultimately, this allows for the exclusion of unnecessary measurements that are implicitly covered by other measurements.

These promises, however, must be interpreted considering the inherent limitations of the chosen theory. DMs are primarily a mathematical construct used to describe OCV changes over the battery's lifetime. Nonetheless, they are valuable for roughly categorizing the degradation mechanisms occurring within the battery. For instance, electrolyte decomposition can be mainly attributed to LLI, while lithium plating affects both LLI and $\mathrm{LAM_{NE}}$ [62]. In this study, we limited the DMs to LLI, $\mathrm{LAM_{NE}}$, and $\mathrm{LAM_{PE}}$, although impedance rise is also a critical factor for battery performance over its lifetime. Impedance significantly impacts the available power of the system, especially in BEV applications, and thus affects fast-charging performance. Future studies should expand the DM terminology to include impedance rise to account for practical performance considerations.

Apart from that, TL opens the possibility to develop many SOH or SOC estimation algorithms by using synthetic data as the source domain. The proposed method can be extended to hysteresis-affected battery cells, such as LFP cells or those with a high silicon content in the anode, by substituting the pseudo-OCV with galvanostatic intermittent titration technique (GITT) measurements. This substitution results in even more pronounced cost and time savings.

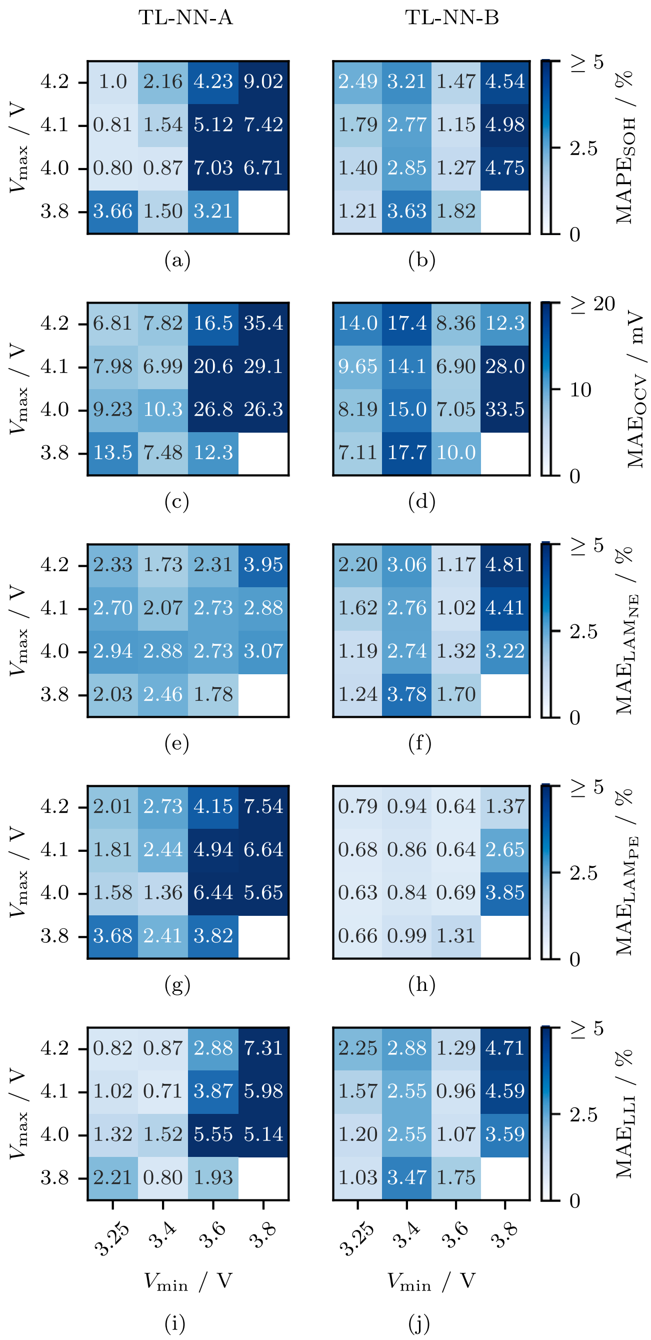

Fig. B.14. SOH estimation, DM estimation and OCV reconstruction accuracy for model TL-NN-A and TL-NN-B for UC1B and varying partial voltage input charging curves. The Subfigures show in detail the $MAPE_{SOH}$ for (a) TL-NN-A and (b) TL-NN-B, the MAE_{OCV} for (c) TL-NN-A and (d) TL-NN-B, the $MAE_{LAM\text{-}NE}$ for (e) TL-NN-A and (f) TL-NN-B, the $MAE_{LAM\text{-}PE}$ for (g) TL-NN-A and (h) TL-NN-B, and the MAE_{LLI} for (i) TL-NN-A and (j) TL-NN-B.

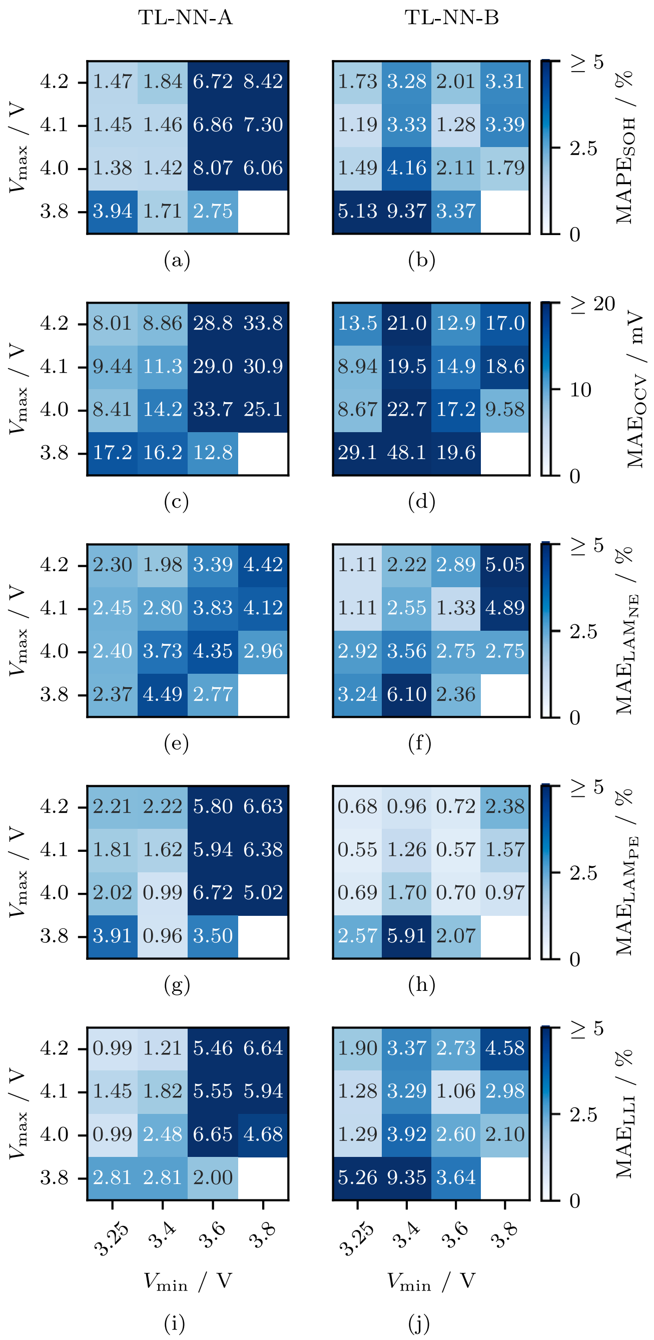

Fig. B.15. SOH estimation, DM estimation and OCV reconstruction accuracy for model TL-NN-A and TL-NN-B for UC2B and varying partial voltage input charging curves. The Subfigures show in detail the $MAPE_{SOH}$ for (a) TL-NN-A and (b) TL-NN-B, the MAE_{OCV} for (c) TL-NN-A and (d) TL-NN-B, the $MAE_{LAM\text{-}NE}$ for (e) TL-NN-A and (f) TL-NN-B, the $MAE_{LAM\text{-}PE}$ for (g) TL-NN-A and (h) TL-NN-B, and the MAE_{LLI} for (i) TL-NN-A and (j) TL-NN-B.

5. Conclusion

This study compares two approaches – TL and optimization – to couple synthetic data for battery state estimation. A base model is trained with a large synthetic dataset, including constant-current charging profiles at various C-rates and degradation states for a large-format automotive NCA-graphite cell. Two TCN-LSTM models are developed: TL-NN-A for estimating OCV and TL-NN-B for estimating alignment parameters from partial voltage segments. These models are fine-tuned with experimental data from a commercial NMC-silicone/graphite cell.

Both models achieve high accuracy, maintaining MAE_{OCV} below 10 mV and $MAPE_{SOH}$ under 2 %, for most use cases even for voltage segments of 200 mV. For the challenging use case with less degradation data, the MAE_{OCV} ranges from 9.23 mV to 19.7 mV, and $MAPE_{SOH}$ ranges from 1.15 % to 2.65 %. Our findings suggest that fine-tuning with one cell from one aging experiment is sufficient if the cell shows the highest

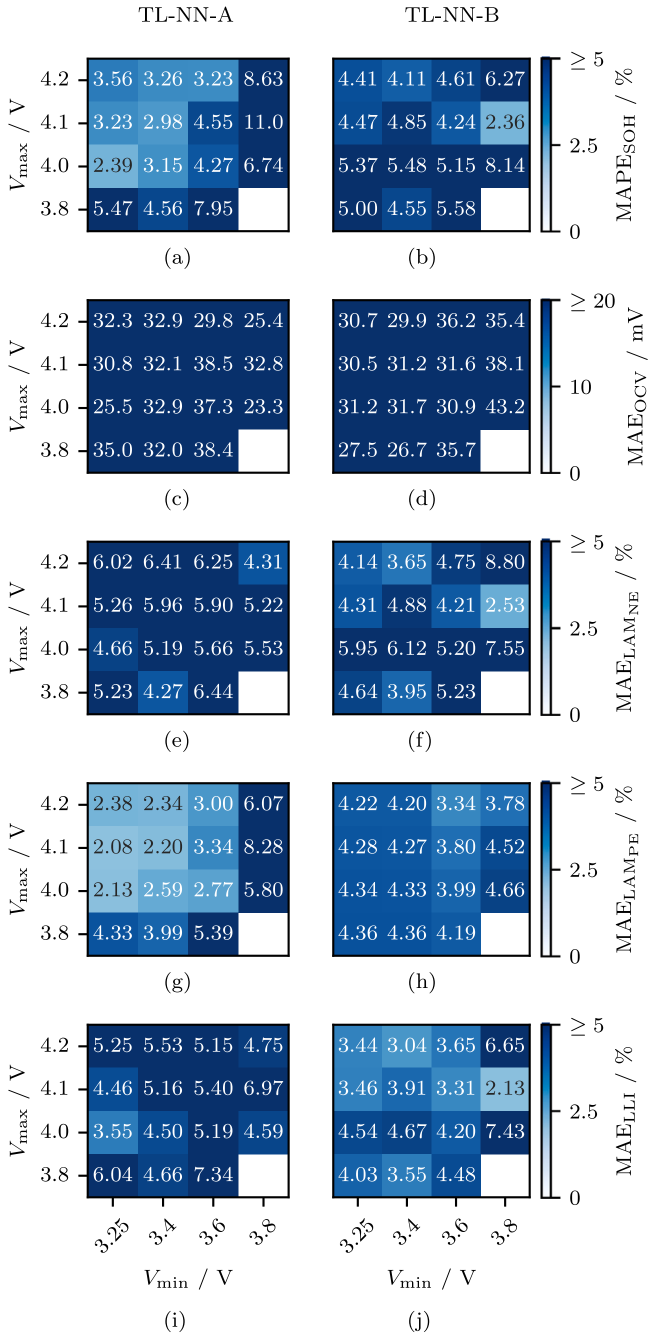

Fig. B.16. SOH estimation, DM estimation and OCV reconstruction accuracy for model TL-NN-A and TL-NN-B for UC3B and varying partial voltage input charging curves. The Subfigures show in detail the MAPE$_{SOH}$ for (a) TL-NN-A and (b) TL-NN-B, the MAE$_{OCV}$ for (c) TL-NN-A and (d) TL-NN-B, the MAE$_{LAM\text{-}NE}$ for (e) TL-NN-A and (f) TL-NN-B, the MAE$_{LAM\text{-}PE}$ for (g) TL-NN-A and (h) TL-NN-B, and the MAE$_{LLI}$ for (i) TL-NN-A and (j) TL-NN-B.

degradation in terms of capacity fade and all DMs. Specific triggering of isolated DMs is not necessary; instead, data generation should focus on evenly developed DMs. Lower cutoff voltages generally lead to better results due to more detectable gradient changes. While TL-NN-B has lower computational requirements and achieves slightly better results, TL-NN-A offers lower data requirements.

Utilizing TL from synthetic data has proven effective for developing battery state estimation models with minimal fine-tuning data. The key to this efficiency is the use of a single aging path with the highest degradation, allowing the model to capture essential features of battery degradation without extensive data. Coupling ML with optimization enables the generation of DMs and the creation of aging-path-specific OCV updates, crucial for optimized battery management systems.

Challenges remain in deploying the coupled model for vehicle applications. It is unclear whether ML can handle noisy and superimposed battery pack signals from multiple cells. Additionally, generalizing the ML model from accelerated lab aging data to real-world aging behavior needs validation. The validity of the assumed ground truth labels of the experimental data can be questioned, but generating the DMs via OCV fits is currently the only available method for non-invasive, reproducible long-term aging tests [63,64]. Future research should explore alternative approaches to combine ML and optimization. For instance, leveraging fleet data to train a Bayesian neural network could constrain the solution space during OCV reconstruction, increasing the likelihood of returning the global optimum.

CRediT authorship contribution statement

Tobias Hofmann: Writing – original draft, Visualization, Validation, Software, Methodology, Investigation, Conceptualization. **Jacob Hamar:** Writing – review & editing, Supervision. **Bastian Mager:** Writing – review & editing, Validation, Methodology. **Simon Erhard:** Writing – review & editing, Supervision. **Jan Philipp Schmidt:** Writing – review & editing, Supervision.

Declaration of competing interest

The authors declare that they have no known competing financial interests or personal relationships that could have appeared to influence the work reported in this paper.

Acknowledgments

Funded by the Open Access Publishing Fund of the University of Bayreuth. This work was performed in cooperation with the University of Bayreuth - Chair of Systems Engineering for Electrical Energy Storage and BMW Group. The authors would like to thank the team of Batemo GmbH for providing the Batemo Cell Models as high-precision physical battery cell models to generate the simulation data.

Appendix A. Neural network optimization and fine-tuning

See Table A.7.

Table A.7
Final number of epochs before the early stopping criterion was fulfilled during the fine-tuning process of the TL models TL-NN-A and TL-NN-B.

Use case	TL-NN-A	TL-NN-B
UC1A	359	524
UC1B	450	490
UC2A	610	1000
UC2B	829	1000
UC3A	521	873
UC3B	614	988

Appendix B. Detailed benchmark results

B.1. Use case 1

See Figs. B.12–B.14.

B.2. Use case 2

See Fig. B.15.

B.3. Use case 3

See Fig. B.16.

Data availability

Data will be made available on request.

References

[1] Şimşir M, Ghayth A. Global trends in electric vehicle battery efficiency and impact on sustainable grid. Sol Energy Sustain Dev J 2024;13(2):1–17. http://dx.doi.org/10.51646/jsesd.v13i2.202.

[2] Sauer DU, Bopp G, Jossen A, Garche J, Rothert M, Wollny M. State of charge — What do we really speak about. In: The 21st international telecommunications energy conference. 1999, p. 6–9.

[3] Plett GL. Extended Kalman filtering for battery management systems of LiPB-based HEV battery packs: Part 2. Modeling and identification. J Power Sources 2004;134(2):262–76. http://dx.doi.org/10.1016/j.jpowsour.2004.02.032.

[4] Plett GL. Extended Kalman filtering for battery management systems of LiPB-based HEV battery packs: Part 3. State and parameter estimation. J Power Sources 2004;134(2):277–92. http://dx.doi.org/10.1016/j.jpowsour.2004.02.033.

[5] Dubarry M, Truchot C, Liaw BY. Synthesize battery degradation modes via a diagnostic and prognostic model. J Power Sources 2012;219:204–16. http://dx.doi.org/10.1016/j.jpowsour.2012.07.016.

[6] Attia PM, Bills A, Planella FB, Dechent P, d. Reis G, Dubarry M, et al. Review—Knees in lithium-ion battery aging trajectories. J Electrochem Soc 2022;169(6):060517. http://dx.doi.org/10.1149/1945-7111/ac6d13.

[7] Bockrath S, Waldhör S, Ludwig H, Lorentz V. State of health estimation using a temporal convolutional network for an efficient use of retired electric vehicle batteries within second-life applications. In: Artificial intelligence for digitising industry–applications. 2022, p. 21–34, River Publishers.

[8] Bockrath S, Lorentz V, Pruckner M. State of health estimation of lithium-ion batteries with a temporal convolutional neural network using partial load profiles. Appl Energ 2023;329:120307. http://dx.doi.org/10.1016/j.apenergy.2022.120307.

[9] Costa N, Sánchez L, Anseán D, Dubarry M. Li-ion battery degradation modes diagnosis via convolutional neural networks. J Energy Storage 2022;55(C):105558. http://dx.doi.org/10.1016/j.est.2022.105558.

[10] Hofmann T, Hamar J, Rogge M, Zoerr C, Erhard S, Schmidt JP. Physics-informed neural networks for state of health estimation in lithium-ion batteries. J Electrochem Soc 2023;170:090524. http://dx.doi.org/10.1149/1945-7111/acf0ef.

[11] Lee S, Kim Y. Li-ion battery electrode health diagnostics using machine learning. In: American control conference. 2020, p. 1137–42. http://dx.doi.org/10.23919/ACC45564.2020.9147633.

[12] Dubarry M, Costa N, Matthews D. Data-driven direct diagnosis of li-ion batteries connected to photovoltaics. Nat Commun 2023;14:3138. http://dx.doi.org/10.1038/s41467-023-38895-7.

[13] Zhang L, Zhang J, Gao T, Lyu L, Wang L, Shi W, et al. Improved LSTM based state of health estimation using random segments of the charging curves for lithium-ion batteries. J Energy Storage 2023;74(B):109370. http://dx.doi.org/10.1016/j.est.2023.109370.

[14] Yao J, Han T. Data-driven lithium-ion batteries capacity estimation based on deep transfer learning using partial segment of charging/discharging data. Energy 2023;271:127033. http://dx.doi.org/10.1016/j.energy.2023.127033.

[15] Zhou Z, Liu Y, Zhang C, Shen W, Xiong R. Deep neural network-enabled battery open-circuit voltage estimation based on partial charging data. J Energy Chem 2024;90:120–32. http://dx.doi.org/10.1016/j.jechem.2023.11.009.

[16] Chen J, Han X, Sun T, Zheng Y. Analysis and prediction of battery aging modes based on transfer learning. Appl Energy 2024;356:122330. http://dx.doi.org/10.1016/j.apenergy.2023.122330.

[17] Hofmann T, Hamar J, Mager B, Erhard S, Schmidt JP. Transfer learning from synthetic data for open-circuit voltage curve reconstruction and state of health estimation of lithium-ion batteries from partial charging segments. Energy AI 2024;17:100382. http://dx.doi.org/10.1016/j.egyai.2024.100382.

[18] Zou G, Yan Z, Zhang C, Song L. Transfer learning with CNN-LSTM model for capacity prediction of lithium-ion batteries under small sample. J Physics: Conf Ser 2022;2258:012042. http://dx.doi.org/10.1088/1742-6596/2258/1/012042.

[19] Sahoo S, Hariharan KS, Agarwal S, Swernath SB, Bharti R, Han S, et al. Transfer learning based generalized framework for state of health estimation of li-ion cells. Sci Rep 2022;12:13173. http://dx.doi.org/10.1038/s41598-022-16692-4.

[20] Shen S, Sadoughi M, Li M, Wang Z, Hu C. Deep convolutional neural networks with ensemble learning and transfer learning for capacity estimation of lithium-ion batteries. Appl Energy 2020;260:114296. http://dx.doi.org/10.1016/j.apenergy.2019.114296.

[21] Chen X, Sun T, Lai X, Zheng Y, Han Xuebing. Transfer learning strategies for lithium-ion battery capacity estimation under domain shift differences. J Energy Storage 2024;90(A):111860. http://dx.doi.org/10.1016/j.est.2024.111860.

[22] Fu S, Tao S, Fan H, He K, Liu X, Tao Y, et al. Data-driven capacity estimation for lithium-ion batteries with feature matching based transfer learning method. Appl Energy 2024;353(A):121991. http://dx.doi.org/10.1016/j.apenergy.2023.121991.

[23] Huang K, Yao K, Guo Y, Lv Z. State of health estimation of lithium-ion batteries based on fine-tuning or rebuilding transfer learning strategies combined with new features mining. Energy 2023;282:128739. http://dx.doi.org/10.1016/j.energy.2023.128739.

[24] Sun Y, Tian H, Hu F, Du J. Method for evaluating degradation of battery capacity based on partial charging segments for multi-type batteries. Batteries 2024;10:187. http://dx.doi.org/10.3390/batteries10060187.

[25] Tian J, Xiong R, Shen W, Lu J, Yang X-G. Deep neural network battery charging curve prediction using 30 points collected in 10 min. Joule 2021;6(5):1521–34. http://dx.doi.org/10.1016/j.joule.2021.05.012.

[26] Tian J, Ma L, Zhang T, Han T, Mai W, Chung CY. Exploiting domain knowledge to reduce data requirements for battery health monitoring. Energy Storage Mater 2024;67:103270. http://dx.doi.org/10.1016/j.ensm.2024.103270.

[27] Hofmann T, Li J, Hamar J, Erhard S, Schmidt JP. The ΔQ-method: State of health and degradation mode estimation for lithium-ion batteries using a mechanistic model with relaxed voltage points. J Power Sources 2024;596:234107. http://dx.doi.org/10.1016/j.jpowsour.2024.234107.

[28] Schmitt J, Rehm M, Karger A, Jossen A. Capacity and degradation mode estimation for lithium-ion batteries based on partial charging curves at different current rates. J Energy Storage 2023;59:106517. http://dx.doi.org/10.1016/j.est.2022.106517.

[29] Zhu C, Sun L, Chen C, Tian J, Shen W, Xiong R. Lithium-ion battery degradation diagnosis and state-of-health estimation with half cell electrode potential. Electrochim Acta 2023;459:142588. http://dx.doi.org/10.1016/j.electacta.2023.142588.

[30] Yang S, Zhang C, Jiang J, Zhang W, Gao Y, Zhang L. A voltage reconstruction model based on partial charging curve for state-of-health estimation of lithium-ion batteries. J Energy Storage 2021;35:102271. http://dx.doi.org/10.1016/j.est.2021.102271.

[31] Xu X, Xu Z, Wang T, Xu J, Pei L. Open-circuit voltage curve reconstruction for degrading lithium-ion batteries utilizing discrete curve fragments from an online dataset. J Energy Storage 2022;56(B):106003. http://dx.doi.org/10.1016/j.est.2022.106003.

[32] Cui Z, Cui N, Li C, Lu J, Zhang C. Online identification and reconstruction of open-circuit voltage for capacity and electrode aging estimation of lithium-ion batteries. IEEE Trans Ind Electron 2023;70(5):4716–26. http://dx.doi.org/10.1109/TIE.2022.3187596.

[33] Aykol M, Gopal CB, Anapolsky A, Herring PK, van Vlijmen B, Berliner MD, et al. Perspective—Combining physics and machine learning to predict battery lifetime. J Electrochem Soc 2021;168(3):030525. http://dx.doi.org/10.1149/1945-7111/abec55.

[34] Liang Y, Wang S, Fan Y, Hao X, Liu D, Fernandez C. State of health prediction of lithium-ion batteries using combined machine learning model based on nonlinear constraint optimization. J Electrochem Soc 2024;171(1):010508. http://dx.doi.org/10.1149/1945-7111/ad18e1.

[35] Tian J, Xiong R, Shen W, Sun F. Electrode ageing estimation and open circuit voltage reconstruction for lithium ion batteries. Energy Storage Mater 2021;37:283–95. http://dx.doi.org/10.1016/j.ensm.2021.02.018.

[36] Bian X, Wei Z, Li W, Pou J, Sauer DU, Liu L. State-of-health estimation of lithium-ion batteries by fusing an open circuit voltage model and incremental capacity analysis. IEEE Trans Power Electron 2022;37(2):2226–36. http://dx.doi.org/10.1109/TPEL.2021.3104723.

[37] Li W, Chen J, Quade K, Luder D, Gong J, Sauer DU. Battery degradation diagnosis with field data, impedance-based modeling and artificial intelligence. Energy Storage Mater 2022;53:391–403. http://dx.doi.org/10.1016/j.ensm.2022.08.021.

[38] Ruan H, Chen J, Ai W, Wu B. Generalised diagnostic framework for rapid battery degradation quantification with deep learning. Energy AI 2022;9:100158. http://dx.doi.org/10.1016/j.egyai.2022.100158.

[39] Sun S, Zhang H, Ge J, Che L. State-of-health estimation for lithium-ion battery using model-based feature optimization and deep extreme learning machine. J Energy Storage 2023;72(E):108732. http://dx.doi.org/10.1016/j.est.2023.108732.

[40] Narayanan SSS, Thangavel S. Terminal voltage prediction of li-ion batteries using combined neural network and teaching learning based optimization algorithm. Appl Soft Comput 2023;133:109954. http://dx.doi.org/10.1016/j.asoc.2022.109954.

[41] Guo R, Xu Y, Hu C, Shen W. A curve relocation approach for robust battery open circuit voltage reconstruction and capacity estimation based on partial charging data. IEEE Trans Power Electron 2024;39(3):3760–73. http://dx.doi.org/10.1109/TPEL.2023.3347236.

[42] Nocedal J, Wright SJ. Numerical optimization. 2nd ed.. Springer; 2006, http://dx.doi.org/10.1007/978-0-387-40065-5.

[43] Tan C, Sun F, Kong T, Zhang W, Yang C, Liu C. A survey on deep transfer learning. In: Artificial neural networks and machine learning – ICANN. 2018, p. 11141. http://dx.doi.org/10.1007/978-3-030-01424-7_27.

[44] Weber M, Auch M, Doblander C, Mandl P, Jacobsen H-A. Transfer learning with time series data: A systematic mapping study. IEEE Access 2021;9:165. http://dx.doi.org/10.1109/ACCESS.2021.3134628.

[45] Hyndman RJ, Koehler AB. Another look at measures of forecast accuracy. Int J Forecast 2006;22–4:679–88. http://dx.doi.org/10.1016/j.ijforecast.2006.03.001.

[46] Schmitt J, Schindler M, Jossen A. Change in the half-cell open-circuit potential curves of silicon–graphite and nickel-rich lithium nickel manganese cobalt oxide during cycle aging. J Power Sources 2021;506:230240. http://dx.doi.org/10.1016/j.jpowsour.2021.230240.

[47] Schmitt J, Schindler M, Oberbauer A, Jossen A. Determination of degradation modes of lithium-ion batteries considering aging-induced changes in the half-cell open-circuit potential curve of silicon–graphite. J Power Sources 2022;532:231296. http://dx.doi.org/10.1016/j.jpowsour.2022.231296.

[48] Bin-Mat-Arishad I, Wimarshana B, Fly A. Influence of voltage profile and fitting technique on the accuracy of lithium-ion battery degradation identification through the voltage profile model. J Energy Storage 2023;70:107884. http://dx.doi.org/10.1016/j.est.2023.107884.

[49] Virtanen P, Gommers R, Oliphant TE, Haberland M, Reddy T, Cournapeau D, et al. SciPy 1.0 contributors, SciPy 1.0: Fundamental algorithms for scientific computing in Python. Nature Methods 2020;17(3):261–72, https://rdcu.be/b08Wh.

[50] Li C, Han X, Zhang Q, Li M, Rao Z, Liao W, et al. State-of-health and remaining-useful-life estimations of lithium-ion battery based on temporal convolutional network-long short-term memory. J Energy Storage 2023;74(Part B):109498. http://dx.doi.org/10.1016/j.est.2023.109498.

[51] Liu S, Chen Z, Yuan L, Xu Z, Jin L, Zhang C. State of health estimation of lithium-ion batteries based on multi-feature extraction and temporal convolutional network. J Energy Storage 2024;75:109658. http://dx.doi.org/10.1016/j.est.2023.109658.

[52] Zhou D, Li Z, Zhu J, Zhang H, Hou L. State of health monitoring and remaining useful life prediction of lithium-ion batteries based on temporal convolutional network. IEEE Access 2020;8:53307–20. http://dx.doi.org/10.1109/ACCESS.2020.2981261.

[53] Zhou D, Wang B. Battery health prognosis using improved temporal convolutional network modeling. J Energy Storage 2022;51:104480. http://dx.doi.org/10.1016/j.est.2022.104480.

[54] Bai S, Kolter JZ, Koltun V. An empirical evaluation of generic convolutional and recurrent networks for sequence modeling. 2018, http://dx.doi.org/10.48550/arXiv.1803.01271, arXiv preprint.

[55] Xu H, Wu L, Xiong S, Li W, Garg A, Gao L. An improved CNN-LSTM model-based state-of-health estimation approach for lithium-ion batteries. Energy 2023;276:127585. http://dx.doi.org/10.1016/j.energy.2023.127585.

[56] Victoria AH, Maragatham G. Automatic tuning of hyperparameters using Bayesian optimization. Evol Syst 2021;12:217–23. http://dx.doi.org/10.1007/s12530-020-09345-2.

[57] O'Malley T, Bursztein E, Long J, Chollet F, Jin H, Invernizzi L, et al. Keras tuner, GitHub. 2019, https://github.com/keras-team/keras-tuner.

[58] Kingma DP, Ba J. Adam: A method for stochastic optimization. 2014, http://dx.doi.org/10.48550/arXiv.1412.6980, arXiv, arXiv:1412.6980.

[59] Rogge M, Jossen A. Path-dependent ageing of lithium-ion batteries and implications on the ageing assessment of accelerated ageing tests. Batter Supercaps 2024;7:e202300313. http://dx.doi.org/10.1002/batt.202300313.

[60] Abdallah ZS, Du L, Webb GI. Data preparation. In: Encyclopedia of machine learning and data mining. 2016, p. 318–27. http://dx.doi.org/10.1007/978-1-4899-7502-7_62-1.

[61] Schmalstieg J, Käbitz S, Ecker M, Sauer DU. A holistic aging model for li(NiMnCo) O2 based 18650 lithium-ion batteries. J Power Sources 2014;257:325–34. http://dx.doi.org/10.1016/j.jpowsour.2014.02.012.

[62] Birkl CR, Roberts MR, McTurk E, Bruce PG, Howey DA. Degradation diagnostics for lithium ion cells. J Power Sources 2017;341:373–86. http://dx.doi.org/10.1016/j.jpowsour.2016.12.011.

[63] Sieg J, Schmid AU, Rau L, Gesterkamp A, Storch M, Spier B, et al. Fast-charging capability of lithium-ion cells: Influence of electrode aging and electrolyte consumption. Appl Energy 2022;305:117747. http://dx.doi.org/10.1016/j.apenergy.2021.117747.

[64] Epding B, Broda A, Rumberg B, Jahnke H, Kwade A. Development of durable 3-electrode lithium-ion pouch cells with LTO reference mesh: Aging and performance studies. J Electrochem Soc 2019;166(8):A1550. http://dx.doi.org/10.1149/2.0851908jes.